Geophysical Journal International

Geophys. J. Int. (2023) **234,** 404–426
Advance Access publication 2023 February 14
GJI Seismology

https://doi.org/10.1093/gji/ggad053

Comparison of methods for coupled earthquake and tsunami modelling

Lauren S. Abrahams [1], Lukas Krenz,[2] Eric M. Dunham [1,3], Alice-Agnes Gabriel [4,5] and Tatsuhiko Saito [6]

[1] *Department of Geophysics, Stanford University, Stanford, CA* 94305*, USA. E-mail: labrahams813@gmail.com*
[2] *Department of Informatics, Technical University of Munich, Munich* 80333*, Germany*
[3] *Institute for Computational and Mathematical Engineering, Stanford University, Stanford, CA* 94305*, USA*
[4] *Department of Earth and Environmental Sciences, Ludwig-Maximilians-Universität München, Munich* 80539*, Germany*
[5] *Institute of Geophysics and Planetary Physics, Scripps Institution of Oceanography, UC San Diego, La Jolla, CA* 92037*, USA*
[6] *National Research Institute for Earth Science and Disaster Resilience, Tsukuba, Ibaraki* 305-0006*, Japan*

Accepted 2023 February 2. Received 2022 December 19; in original form 2022 July 7

SUMMARY

Tsunami generation by offshore earthquakes is a problem of scientific interest and practical relevance, and one that requires numerical modelling for data interpretation and hazard assessment. Most numerical models utilize two-step methods with one-way coupling between separate earthquake and tsunami models, based on approximations that might limit the applicability and accuracy of the resulting solution. In particular, standard methods focus exclusively on tsunami wave modelling, neglecting larger amplitude ocean acoustic and seismic waves that are superimposed on tsunami waves in the source region. In this study, we compare four earthquake-tsunami modelling methods. We identify dimensionless parameters to quantitatively approximate dominant wave modes in the earthquake-tsunami source region, highlighting how the method assumptions affect the results and discuss which methods are appropriate for various applications such as interpretation of data from offshore instruments in the source region. Most methods couple a 3-D solid earth model, which provides the seismic wavefield or at least the static elastic displacements, with a 2-D depth-averaged shallow water tsunami model. Assuming the ocean is incompressible and tsunami propagation is negligible over the earthquake duration leads to the instantaneous source method, which equates the static earthquake seafloor uplift with the initial tsunami sea surface height. For longer duration earthquakes, it is appropriate to follow the time-dependent source method, which uses time-dependent earthquake seafloor velocity as a forcing term in the tsunami mass balance. Neither method captures ocean acoustic or seismic waves, motivating more advanced methods that capture the full wavefield. The superposition method of Saito *et al*. solves the 3-D elastic and acoustic equations to model the seismic wavefield and response of a compressible ocean without gravity. Then, changes in sea surface height from the zero-gravity solution are used as a forcing term in a separate tsunami simulation, typically run with a shallow water solver. A superposition of the earthquake and tsunami solutions provides an approximation to the complete wavefield. This method is algorithmically a two-step method. The complete wavefield is captured in the fully coupled method, which utilizes a coupled solid Earth and compressible ocean model with gravity. The fully coupled method, recently incorporated into the 3-D open-source code SeisSol, simultaneously solves earthquake rupture, seismic waves and ocean response (including gravity). We show that the superposition method emerges as an approximation to the fully coupled method subject to often well-justified assumptions. Furthermore, using the fully coupled method, we examine how the source spectrum and ocean depth influence the expression of oceanic Rayleigh waves. Understanding the range of validity of each method, as well as its computational expense, facilitates the selection of modelling methods for the accurate assessment of earthquake and tsunami hazards and the interpretation of data from offshore instruments.

Key words: Tsunamis; Computational seismology; Guided waves; Wave propagation; Mechanics, theory and modelling; Subduction zone processes.

1 INTRODUCTION

Computational modelling coupling the solid Earth and ocean is crucial for studying earthquake-driven tsunami generation. Applications include interpreting data from actual events (Tanioka & Sataka 1996; Fujii & Satake 2007; Simons *et al.* 2011; Yamazaki *et al.* 2018), informing tsunami early warning (Liu *et al.* 2009; Bernard & Titov 2015; Selva *et al.* 2021) and performing scenario modelling of subduction events (Witter *et al.* 2013; Hayes *et al.* 2014; LeVeque *et al.* 2016; Baba *et al.* 2016; Goda *et al.* 2017; Grezio *et al.* 2017; Scala *et al.* 2020) and offshore strike-slip events (Ulrich *et al.* 2019; Krenz *et al.* 2021; Elbanna *et al.* 2021; Amlani *et al.* 2022). Earthquakes excite a rich variety of waves in the solid Earth and ocean, including seismic waves, ocean acoustic waves and surface gravity waves (tsunamis). The modelling of wave generation and propagation in a compressible ocean with gravity has a long history (Stoneley 1926; Sells 1965; Kajiura 1970; Duffy 1992; Nosov 1999; Levin *et al.* 2009), with recent advances focused more on algorithms and workflows for forward models and data inversion in realistically complex geometries. Certain applications focus on just one of these waves, for example, surface gravity waves for tsunami hazard assessment or seismic waves for traditional earthquake source characterization. However, other applications require or at least benefit from the modelling of more than one wave type. For example, joint inversion of seismic and tsunami data provides the best constraints on the rupture process of the 2011 Tohoku-Oki event (Yokota *et al.* 2011; Yamazaki *et al.* 2018; Lay 2018), resolving inconsistencies between inversions of only seismic, geodetic or tsunami data (Lay *et al.* 2011; Satake *et al.* 2013). In particular, tsunami data can place much tighter constraints on the extent of shallow slip than seismic and geodetic data, which is critical for understanding tsunamigenesis (DeDontney & Rice 2012; Cheung *et al.* 2022; Mulia *et al.* 2022; Ye *et al.* 2022). In addition, new offshore instrument networks over earthquake source regions, such as DONET in the Nankai Trough (Kawaguchi *et al.* 2008) and S-net in the Japan Trench (Yamamoto *et al.* 2016), have demonstrated that the wavefield is a complex superposition of all of the previously mentioned wave types. Fibre optic technologies offer much promise for densely sampling this complex offshore wavefield (Lindsey *et al.* 2019; Sladen *et al.* 2019; Zhan *et al.* 2021). While filtering approaches can be applied to isolate certain waves (Tsushima *et al.* 2012; Saito & Tsushima 2016), the best constraints on the source will be obtained from models that capture all waves. This has motivated the development of new, coupled solid Earth and ocean modelling methods. Other methods utilize a one-way coupling from the solid Earth to the ocean. Some of these account for the time dependence of the seafloor displacement, while others use the static displacement. All of these methods utilize simplifying assumptions, often providing simpler modelling workflows or more efficient computations. However, these assumptions can limit the applicability of the given method.

The purpose of this study is to examine four modelling methods to assess the consequences of the approximations and the relevance of each method to various features of interest in the wavefield. In this study, we use the Lotto & Dunham (2015) method for fully coupled earthquake and tsunami modelling, which was recently extended from 2-D to 3-D by Krenz *et al.* (2021) through an implementation in the open-source code SeisSol (Dumbser & Käser 2006; Pelties *et al.* 2014; Breuer *et al.* 2015; Uphoff *et al.* 2017). We present verification tests of the fully coupled approach against an exact solution. Together with shallow water solvers, the SeisSol implementation provides us simulation capabilities for all four modelling methods. We compare these modelling methods in three ways. First, we focus on the ocean response to a specified seafloor displacement. This is done analytically using seafloor-to-sea surface frequency-domain transfer functions (Section 3), which highlight the different wave modes that contribute to the overall wavefield, as well as through time-domain numerical simulations (Section 4). Next, we study the more realistic problem of wave generation and propagation from earthquake ruptures using SeisSol dynamic rupture simulations in a coupled ocean-solid earth model. In addition to comparing the modelling methods for this problem (Section 5), we identify and discuss prominent features of the seismic and acoustic wavefield. In particular, we examine how the source spectrum and ocean depth influence the expression of oceanic Rayleigh waves (Section 6).

The most widely used method for modelling tsunami generation is equating the final, or static, vertical seafloor displacement from the earthquake to the initial sea surface uplift, which serves as the initial condition for a tsunami model. This equivalence arises from the assumption of a hydrostatic ocean response, which is justified when the horizontal wavelengths of the seafloor displacement are large compared to ocean depth. These are the same conditions that justify use of the shallow water model for tsunami propagation. However, short wavelength seafloor perturbations, particularly in deep water like that characterizing many subduction zone trench regions, cause a non-hydrostatic response. Kajiura (1963) has shown how this effectively filters the short wavelength features of the seafloor displacement from the sea surface response.

In addition, using the static seafloor displacement to set initial conditions for the tsunami model assumes that tsunami propagation is negligible over rupture duration, a condition that is justified for many earthquakes (Kajiura 1963; Ward 2001; Tanioka & Seno 2001; Saito & Furumura 2009). This is the basis for the widely used workflow of computing seafloor uplift from static elastic solutions for fault slip, such as the solutions of Okada (1985) for dislocations in a homogeneous elastic half-space. However, for long-duration tsunami earthquakes, extremely large earthquakes and underwater landslides, tsunamis can propagate over distances comparable to or exceeding the horizontal wavelengths of the seafloor displacement while the seafloor is still deforming. This has motivated tsunami models with a time-dependent source term describing seafloor uplift added to the mass balance (Kajiura 1970). Recent modelling studies have explored the importance of accounting for time-dependent seafloor displacements for accurate tsunami modelling (Kervella *et al.* 2007; Saito & Furumura 2009; Madden *et al.* 2021).

Both of these methods assume that the ocean is incompressible, thereby neglecting ocean acoustic wave generation and propagation. This assumption is justified when interpreting data far from the source region because the acoustic waves propagate much faster than the tsunami, allowing a clear separation of these waves. However, the deployment of pressure gauges and ocean bottom seismometers in the offshore region above or adjacent to earthquake sources has shown the superposition of tsunami waves, seismic waves and

ocean acoustic waves (Nosov & Kolesov 2007; Matsumoto *et al.* 2017; Saito *et al.* 2019; Kubota *et al.* 2021). This has motivated the development of new methods that aim to capture the full wavefield. We note that several fully coupled modelling methods were developed decades ago in the context of mode summation for plane-layered or spherically symmetric earth models with a compressible ocean subject to gravity (Ward 1980, 1981; Comer 1984; Dahlen & Tromp 1999). In comparison, the new methods we focus on here have arisen independently as extensions of 2-D and 3-D seismic wave propagation (and in some cases earthquake dynamic rupture) codes that can handle the material heterogeneity and complex seafloor bathymetry existing in real subduction zones.

Maeda & Furumura (2013) were the first to introduce a fully coupled modelling method by adding gravity to their seismic and acoustic wave propagation code for solid Earth and the ocean. Lotto & Dunham (2015) provided an alternative framework for fully coupled modelling, starting from the linearized governing equations for small perturbations of a compressible ocean about an initial hydrostatic rest state. They implemented this model in a 2-D finite difference code for both kinematic and dynamic earthquake ruptures (Lotto & Dunham 2015; Lotto *et al.* 2017, 2018). This method was also successfully implemented in 2-D and 3-D finite element codes (Wilson & Ma 2021; Ma 2022). The methods of both Maeda & Furumura (2013) and Lotto & Dunham (2015) simultaneously model all waves in one simulation. We note that the governing equations of Maeda & Furumura (2013) differ from those of Lotto & Dunham (2015); the former appear not to have received continued use in the literature so they will not be explored in our study.

In contrast to the fully coupled modelling methods, Saito *et al.* (2019) have introduced a two-step sequential modelling method for the same problem. First, the earthquake rupture, seismic waves, and ocean acoustic waves are modelled in a coupled Earth and compressible ocean model without gravity. The sea surface vertical velocity from this model is then used as a source term in an incompressible 2-D tsunami simulation, using some form of a shallow water solver (e.g. non-dispersive linear long wave or weakly dispersive Boussinesq). The appropriate superposition of the earthquake and tsunami solutions provides an approximation to the complete wavefield. (For fields other than the sea surface displacement, this requires computing the 3-D ocean response from the 2-D shallow water solution, using the assumptions that provide the basis of the depth-integrated shallow water model.) Even though the tsunami simulation utilizes an incompressible ocean, this superposition of the earthquake and tsunami solutions accounts for acoustic and seismic waves.

The fully coupled and superposition methods require wave propagation simulations which are computationally expensive and usually require parallel computing in 3-D. The superposition method additionally uses a tsunami simulation to incorporate gravity. This tsunami simulation is 2-D depth-integrated and, for most shallow water models, allows much larger time steps. Hence it has a vastly smaller computational cost than the initial 3-D simulation. Comparing the fully coupled and superposition methods, the addition of gravity adds negligible computational cost. Hence, the superposition method has no real computational advantage over the fully coupled method in modelling the wave generation process. The superposition method offers two possible advantages over the fully coupled method. First, it can be performed using many existing wave propagation codes without needing to introduce a stable and accurate treatment of the free surface boundary condition to account for gravity. Second, it is straightforward to continue running the efficient tsunami simulation for a much longer time than the initial 3-D wave propagation model to study regional or global tsunami propagation as well as inundation (if a non-linear tsunami model is used). Currently, there is no established workflow for transitioning between the fully coupled method solution and a shallow water tsunami simulation.

In this study, we formally establish the relation between the superposition-based method of Saito *et al.* (2019) and the fully coupled method of Lotto & Dunham (2015), showing that their differences are negligibly small in many relevant cases. In addition, we perform verification tests of the recent 3-D implementation by Krenz *et al.* (2021) of the Lotto & Dunham (2015) method to 3-D in the open-source SeisSol code (Dumbser & Käser 2006; Breuer *et al.* 2015; Pelties *et al.* 2014; Uphoff *et al.* 2017). We then use the fully coupled SeisSol solution as a reference solution for comparison to alternative modelling methods. Specifically, we compare results of four modelling methods for a variety of imposed seafloor displacement and earthquake rupture sources. We explore how the wavefield is influenced by the horizontal wavelengths characterizing the source, the source duration, and ocean compressibility. Non-dimensional parameters allow us to quantify the validity of the model assumptions. A comparison of the results reveals discrepancies between the models whenever these assumptions are violated. Understanding the range of validity of each method, as well as its computational expense, facilitates the selection of modelling method for accurate assessment of earthquake and tsunami hazards and the interpretation of data from offshore instruments.

Our earthquake rupture simulations reveal a complex set of ocean acoustic and seismic waves, the most prominent of which we identify as oceanic Rayleigh waves. We examine the dispersion properties of these waves to explain key features of the resulting wavefield, highlighting how the wavefield changes with ocean depth and the frequency band of waves excited by the earthquake source. We anticipate these results to guide interpretation of data from offshore instruments.

2 METHODS FOR COUPLED EARTHQUAKE–TSUNAMI MODELLING

This section outlines the four modelling methods used in this study. Starting with the general problem, we derive the fully coupled method (method 1). Next, we apply approximations to the general problem to derive commonly used shallow water methods (methods 2 and 3) and the recently developed superposition method (method 4). The methods are summarized in Fig. 1. Method 2 assumes an incompressible ocean and that tsunami propagation is negligible over the duration of the earthquake, so that tsunami generation is captured by specifying initial sea surface height in the tsunami model. Often the initial sea surface height is equated to the static seafloor uplift from an earthquake model. In some applications of this method, the seafloor uplift is filtered to remove short wavelength components when translating to initial sea surface height; the filter, referred to as the Kajiura filter, is based on an analytic solution to Laplace's equation for pressure (or velocity potential) in an incompressible ocean of uniform depth and accounts for non-hydrostatic response at short wavelengths (Kajiura 1963, 1970; Tanioka & Satake 1996). For longer-duration earthquakes, it is more appropriate to follow method 3, which uses the time-dependent seafloor velocity from an earthquake model as a time-dependent forcing term in the tsunami mass balance equation (Saito & Furumura 2009; Saito & Tsushima 2016; Saito 2019).

We remark that the shallow water solver used in these two methods can solve either linearized equations, if attention is restricted to

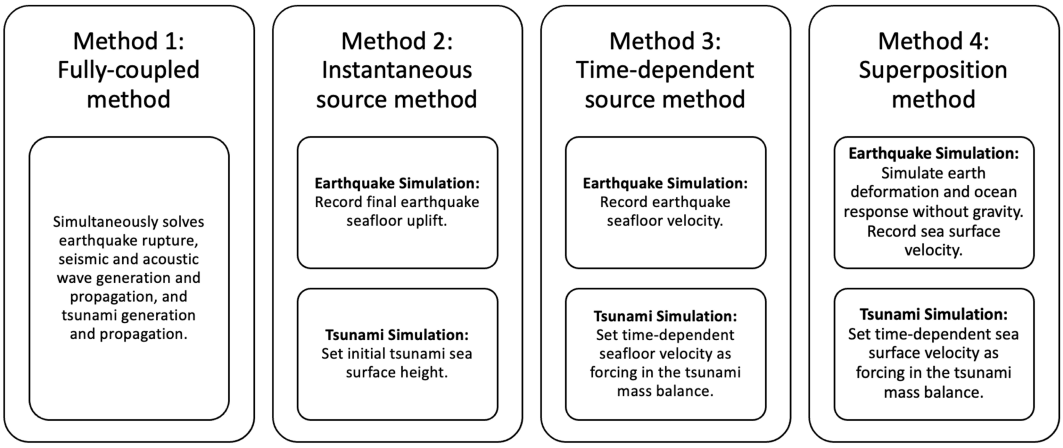

Figure 1. We compare four modelling methods in this paper. Method 1, the fully coupled method, simultaneously solves earthquake rupture and ocean response. Methods 2–4 are two-step methods, using approximations to send information from an earthquake simulation into a separate tsunami simulation. Only methods 1 and 4 capture the full wavefield; methods 2 and 3 are limited to tsunami waves.

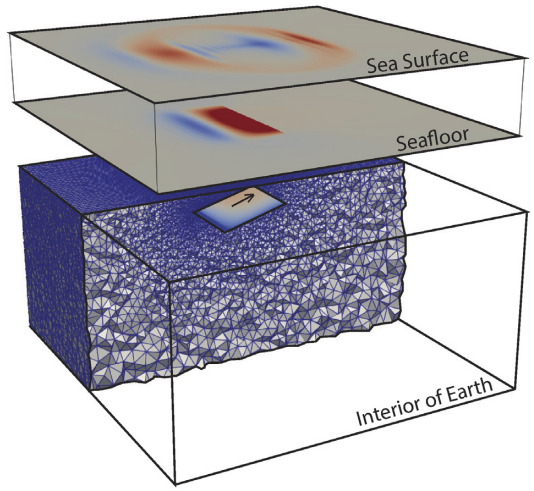

Figure 2. 3-D model domain with an underlying elastic solid and overlying acoustic ocean. The full domain is discretized with an unstructured tetrahedral mesh. Surfaces offset for visualization.

the offshore region, or non-linear equations, for applications involving inundation and run-up and other problems where non-linearities are important. In this study, we limit our attention to the offshore region where the linear shallow water equations are justified. In addition, the effects of dispersion on tsunami propagation can be accounted for approximately with a Boussinesq solver or neglected in the more commonly used linear long wave model.

Neither method 2 nor method 3 captures ocean acoustic or seismic waves, motivating the development of more advanced methods. Saito *et al.* (2019) propose a superposition-based modelling method, referred to here as method 4, which solves the 3-D elastic and acoustic wave equations to model the earthquake rupture, seismic wavefield, and the response of a compressible ocean without gravity. Then, changes in sea surface height from this zero-gravity solution are used as a time-dependent forcing term in a separate, shallow water tsunami simulation. A superposition of the earthquake and tsunami solutions provides the complete wavefield, with some approximations applied to the tsunami propagation problem depending on the shallow water solver used (linear long wave or Boussinesq). Thus, while method 4 is algorithmically a two-step method, like methods 2 and 3, it provides more than just the tsunami wavefield. The complete wavefield is captured in method 1 (Fig. 2), which directly solves the equations governing the response of a fully coupled solid Earth and ocean with gravity (Lotto & Dunham 2015).

2.1 Statement of the general problem

Consider perturbations to an ocean of equilibrium depth $H(x, y)$. The z-axis is vertical and directed upward, opposite to gravity and the unperturbed sea surface is the plane $z = 0$. We use an Eulerian description. We consider first problems in which the seafloor displacement is specified, then replace this with acoustic–elastic interface conditions at the seafloor to couple the ocean to the solid Earth. For the first class of problems, an earthquake, or another source, causes vertical uplift $b(x, y, t)$ of the seafloor, such that the seafloor is now located at $z = -H(x, y) + b(x, y, t)$. The vertical uplift has contributions from both vertical and horizontal displacements (U_i) of the solid Earth if the seafloor is sloped. Tanioka & Satake (1996) introduced the widely used linearized relation,

$$b = U_z + U_x \frac{\partial H}{\partial x} + U_y \frac{\partial H}{\partial y}, \tag{1}$$

which is valid when deformation-induced changes in bathymetry are sufficiently small. The perturbed ocean surface is $z = \eta(x, y, t)$.

In this general problem, the ocean is compressible and inviscid, with gravity acting as a restoring force. Following Lotto & Dunham (2015), the governing equations for small perturbations about an initial hydrostatic equilibrium rest state of the ocean are derived by combining the mass balance (continuity) with a linearized equation of state, yielding

$$\frac{1}{K}\frac{\partial p}{\partial t} + \frac{\partial v_x}{\partial x} + \frac{\partial v_y}{\partial y} + \frac{\partial v_z}{\partial z} = 0, \tag{2}$$

and the momentum balance equations,

$$\rho \frac{\partial v_x}{\partial t} + \frac{\partial p}{\partial x} = 0, \tag{3}$$

$$\rho \frac{\partial v_y}{\partial t} + \frac{\partial p}{\partial y} = 0, \tag{4}$$

and

$$\rho \frac{\partial v_z}{\partial t} + \frac{\partial p}{\partial z} = 0, \tag{5}$$

for particle velocities v_i, pressure perturbation p, bulk modulus K and density ρ. The sound speed is $c_0 = \sqrt{K/\rho}$. We neglect source terms of $\mathcal{O}(g/\omega c_0)$, where ω is the angular frequency characterizing a wave and g is the gravitational acceleration (Lotto & Dunham 2015). The governing equations, as written, can have depth-dependent ρ and K. Accounting for this depth dependence is necessary for a rigorous inclusion of compressibility effects using a linearized equation of state. Instead, we assume in this study that both ρ and K are constants which incurs an error of $\mathcal{O}(gH/c_0^2)$ which is quite small for Earth's oceans and can thus be neglected.

With these approximations, gravity enters only through a linearization of the free surface boundary condition,

$$p - \rho g \eta = 0, \quad \text{at } z = 0. \tag{6}$$

The equations are closed by adding the linearized kinematic condition on the sea surface,

$$\frac{\partial \eta}{\partial t} = v_z, \quad \text{at } z = 0, \tag{7}$$

and, for problems in which the seafloor displacement is specified, the linearized kinematic condition on the seafloor,

$$\frac{\partial b}{\partial t} = v_z + v_x \frac{\partial H}{\partial x} + v_y \frac{\partial H}{\partial y}, \quad \text{at } z = -H. \tag{8}$$

Note that eq. (1) follows directly from time integration of eq. (8). For problems that couple the ocean to the solid Earth, the seafloor kinematic condition is replaced with the following acoustic-elastic interface conditions at the seafloor: (i) continuity of normal displacement, (ii) balancing normal traction on the solid side with pressure on the ocean side and (iii) vanishing shear traction on the solid side.

2.2 Method 1: Fully coupled method

The fully coupled method, which provides a reference solution to which solutions from other methods are compared, is obtained by solving eqs (2)–(7) in the ocean and the elastic wave equation in the solid Earth. The ocean and solid are coupled by enforcing continuity of the normal velocity and traction components of stress across the seafloor interface, rather than imposing the seafloor uplift through the kinematic condition (8).

2.3 Approximations to method 1 (fully coupled method) yield shallow water modelling methods 2 and 3

The most commonly used methods for modelling tsunami generation and propagation couple a 3-D earth model with a 2-D depth-averaged shallow water tsunami model. Starting with the general problem governed by eqs (2)–(8), we make two well-known approximations to obtain the linearized shallow water equations. First, when $\omega H/c_0 \ll 1$, where ω is the angular frequency, the ocean responds in an effectively incompressible manner. This eliminates the $K^{-1}\partial p/\partial t$ term in eq. (2).

We then depth integrate the resulting continuity equation for an incompressible fluid and use the linearized kinematic conditions (7) and (8) to obtain

$$\frac{\partial \eta}{\partial t} + \frac{\partial q_x}{\partial x} + \frac{\partial q_y}{\partial y} = \frac{\partial b}{\partial t}, \tag{9}$$

in which the linearized depth-integrated horizontal velocities, also know as fluxes, are

$$q_x = \int_{-H}^{0} v_x dz, \quad q_y = \int_{-H}^{0} v_y dz. \tag{10}$$

Second, we neglect the inertial term $\rho \partial v_z/\partial t$ in the vertical momentum balance (eq. 5), such that the pressure perturbation p is independent of depth and equal to the hydrostatic pressure change $\rho g \eta$. This is justified when vertical accelerations are small compared to g, which occurs for small-amplitude perturbations when $kH \ll 1$, where k is the horizontal wavenumber characterizing the solution. It then follows from eq. (6) that the horizontal pressure gradient is independent of depth. Thus, the horizontal momentum balances (eqs 3 and 4) become independent of depth, and after depth integration are

$$\frac{\partial q_x}{\partial t} + gH \frac{\partial \eta}{\partial x} = 0 \tag{11}$$

and

$$\frac{\partial q_y}{\partial t} + gH \frac{\partial \eta}{\partial y} = 0. \tag{12}$$

Eqs (9), (11) and (12) are the linear long wave equations that describe non-dispersive tsunami propagation at the shallow water wave speed $(gH)^{1/2}$. These are the equations used in most parts of this study for the shallow water problem.

We remark that effects of dispersion can be approximately accounted for using the Boussinesq approximation (Saito *et al.* 2010; Baba *et al.* 2015, 2017; Saito 2019), which adds non-hydrostatic pressure correction terms to the momentum balances (eqs 11 and 12):

$$\frac{\partial q_x}{\partial t} + gH \frac{\partial \eta}{\partial x} = \frac{1}{3} H^2 \frac{\partial^2}{\partial x \partial t} \left(\frac{\partial q_x}{\partial x} + \frac{\partial q_y}{\partial y} \right) \tag{13}$$

and

$$\frac{\partial q_y}{\partial t} + gH \frac{\partial \eta}{\partial y} = \frac{1}{3} H^2 \frac{\partial^2}{\partial y \partial t} \left(\frac{\partial q_x}{\partial x} + \frac{\partial q_y}{\partial y} \right). \tag{14}$$

We use this Boussinesq model in the final part of our study and compare results to those of the linear long wave model.

2.3.1 Method 2: Instantaneous source method

Method 2 is the simplest and most commonly used two-step method. It is based on the premise that the earthquake source occurs over such short time scales, as compared to tsunami propagation time scales, that the source can be regarded as instantaneous. In this method, an earthquake model is used to provide the static seafloor uplift $b_{st}(x, y)$. This is often computed using dislocation solutions for a uniform elastic half-space, but can also be obtained using the final displacements from a time-dependent kinematic or dynamic rupture simulation. These solutions are typically calculated by neglecting the ocean and by treating the seafloor as a free surface.

Next, a shallow water tsunami simulation is performed by solving eqs (9), (11) and (12), with the forcing term $\partial b/\partial t$ in eq. (9) set to zero and

$$\eta(x, y, 0^+) = b_{st}(x, y), \tag{15}$$

$$q_x(x, y, 0^+) = 0, \tag{16}$$

$$q_y(x, y, 0^+) = 0, \tag{17}$$

as initial condition. Here, $t = 0^+$ corresponds to the end of the earthquake and the start of tsunami propagation. The first initial condition (eq. 15) follows from the time integration of eq. (9) over the earthquake source region, assuming a dominant balance between sea surface uplift rate $\partial\eta/\partial t$ and seafloor uplift rate $\partial b/\partial t$. This is justified when the seafloor displacement occurs over a sufficiently short time scale such that horizontal fluxes are negligible over the earthquake duration, or equivalently when the tsunami propagation distance over the earthquake duration is much shorter than the horizontal wavelengths characterizing the seafloor uplift. Alternatively, one can view the seafloor uplift forcing, at the much longer time scales of the tsunami, as effectively instantaneous by writing

$$\partial b/\partial t \approx b_{st}(x, y)\delta(t); \tag{18}$$

then integrating eq. (9) with this forcing across $t = 0$ yields the initial condition eq. (15).

Setting initial horizontal fluxes to zero (eqs 16 and 17) is justified when the seafloor displacement transfers negligible horizontal momentum, in the form of tsunami waves, to the ocean. While some studies have argued that horizontal momentum transfer may be important (Song *et al.* 2008, 2017; Song & Han 2011), simulations using a 2-D fully coupled model (Lotto *et al.* 2017, 2018) show that it is negligible for the geometries and problems of interest here.

We note that there are variants of method 2 in which $b_{st}(x, y)$ is filtered to account for non-hydrostatic effects at short wavelengths during the tsunami generation process prior to setting the initial condition on $\eta(x, y, 0^+)$ (Kajiura 1963, 1970; Nosov & Kolesov 2011). This is often referred to as the Kajiura filter. Likewise, the tsunami problem can be solved using a non-linear shallow water solver and/or a Boussinesq solver that accounts approximately for tsunami dispersion (Baba *et al.* 2015, 2017; Saito 2019; Saito & Kubota 2020; Du *et al.* 2021).

To summarize, this one-way coupled method assumes that the ocean is incompressible, horizontal wavelengths are much longer compared to ocean depth and tsunami propagation is negligible over the earthquake duration.

2.3.2 *Method 3: Time-dependent source method*

For longer duration sources, horizontal flux terms in the tsunami mass balance are not negligible while the seafloor is actively deforming, and thus, tsunami propagation occurs over the earthquake duration. In this case, the time-dependent forcing term in the mass balance must be used when solving the tsunami problem. Similar to method 2, an earthquake simulation computes $b(x, y, t)$. It is insufficient to only compute the static uplift, $b_{st}(x, y)$. The tsunami solution is obtained by solving the shallow water eqs (9)–(12) with homogeneous initial conditions. Coupling from the earthquake to the tsunami occurs through the forcing term $\partial b/\partial t$ in the mass balance (eq. 9). No forcing is added to the momentum balance equations, consistent with the previously stated assumption of negligible horizontal momentum transfer from the solid Earth to the ocean during seafloor displacement. Note that method 2 is a limiting case of method 3 for sufficiently short duration $\partial b/\partial t$.

The instantaneous source two-step method (method 2) and time-dependent source two-step method (method 3) are generally acceptable for modelling tsunami propagation and are prevalent in current modelling practices. However, they do not include contributions from acoustic waves and cannot be used for certain applications, for example, for improving tsunami early warning approaches. For this purpose, we need models that capture both acoustic and tsunami waves in the ocean.

2.4 Approximations to method 1 (fully coupled method) yields method 4 (superposition method)

The fully coupled method (method 1) provides the full seismic, acoustic, and tsunami wavefield. However, this requires a stable and accurate implementation of the free surface boundary condition with gravity, namely eqs (6) and (7), rather than the usual $p = 0$ free surface condition that is enforced in most 3-D seismic/acoustic wave propagation codes. Code modifications can be avoided using a superposition-based method for computing the full wavefield (Saito 2019; Saito *et al.* 2019). We refer to this superposition method as method 4. Here we show how the superposition method can be obtained from the fully coupled method by making a few approximations that are often well-justified; this connection has not previously been recognized in the literature. The superposition method differs from the fully coupled method in that it is algorithmically a two-step method that must be implemented using two separate codes, a seismic wave propagation code without gravity and a tsunami code. The method passes information from an initial zero-gravity simulation, conducted with a compressible ocean and thus resolving both acoustic and seismic waves, to a tsunami simulation (which, thus far in the literature, has been conducted using incompressible shallow water solvers). The zero-gravity simulation provides a time-dependent forcing term for the tsunami simulation, and an appropriate superposition of the two solutions provides the full wavefield (Saito 2019; Saito *et al.* 2019).

Here we provide a derivation of the superposition method that reduces to the method introduced by Saito *et al.* (2019). We denote by a superscript (1) the zero-gravity solution obtained by solving governing eqs (2)–(5) with boundary conditions (6)–(8), but with $g = 0$ in eq. (6). We denote by a superscript (2) the solution to a second problem that when superimposed with solution 1 yields the exact solution to the fully coupled problem. Thus, the superposition of solutions 1 and 2 provides the full wavefield, which is, by construction, identical to the fully coupled solution.

We next derive the equations and boundary conditions for solution 2. To do this, we write each field as a superposition of the fields from solutions 1 and 2, for example $p = p^{(1)} + p^{(2)}$. Then we subtract the solution 1 governing equations and boundary conditions from those for the full solution (which are identical except for the $\rho g\eta$ term in the top boundary condition). This procedure yields the solution 2 governing equations

$$\frac{1}{K}\frac{\partial p^{(2)}}{\partial t} + \frac{\partial v_x^{(2)}}{\partial x} + \frac{\partial v_y^{(2)}}{\partial y} + \frac{\partial v_z^{(2)}}{\partial z} = 0, \tag{19}$$

$$\rho\frac{\partial v_x^{(2)}}{\partial t} + \frac{\partial p^{(2)}}{\partial x} = 0, \tag{20}$$

$$\rho\frac{\partial v_y^{(2)}}{\partial t} + \frac{\partial p^{(2)}}{\partial y} = 0, \tag{21}$$

$$\rho\frac{\partial v_z^{(2)}}{\partial t} + \frac{\partial p^{(2)}}{\partial z} = 0, \tag{22}$$

and boundary conditions

$$p^{(2)} - \rho g\eta^{(2)} = \rho g\eta^{(1)}, \quad z = 0, \tag{23}$$

$$\frac{\partial \eta^{(2)}}{\partial t} - v_z^{(2)} = 0, \quad z = 0, \tag{24}$$

$$v_z^{(2)} + v_x^{(2)}\frac{\partial H}{\partial x} + v_y^{(2)}\frac{\partial H}{\partial y} = 0, \quad z = -H. \tag{25}$$

Note that solution 2 is forced by the $\rho g \eta^{(1)}$ term in the top boundary condition (eq. 23), and there is no seafloor forcing in eq. (25), as that has been accounted for in solution 1.

Thus far, no approximations have been made, and solving for solution 2 requires exactly the same solver (and involves approximately the same computational cost) as solving the fully coupled problem, including the gravity-related term in eq. (23). It is only by introducing approximations that the superposition method can be performed with minimal additional computational expense as compared to the fully coupled method. The approximations are motivated by the anticipation that solution 2 will be dominated by tsunami waves, with the remainder being (ideally negligible) corrections to the seismic and ocean acoustic waves in solution 1. To examine this, we apply the previously described set of shallow water approximations (incompressibility and depth-independent hydrostatic pressure changes) to the governing equation of solution 2. We denote the approximate solution 2 with a superscript $(2')$, which can be obtained with a shallow water solver.

With these approximations, solution $2'$ is determined by the linear long wave equations

$$\frac{\partial \eta^{(2')}}{\partial t} + \frac{\partial q_x^{(2')}}{\partial x} + \frac{\partial q_y^{(2')}}{\partial y} = 0, \tag{26}$$

$$\frac{\partial q_x^{(2')}}{\partial t} + gH\frac{\partial \eta^{(2')}}{\partial x} = -gH\frac{\partial \eta^{(1)}}{\partial x}, \tag{27}$$

$$\frac{\partial q_y^{(2')}}{\partial t} + gH\frac{\partial \eta^{(2')}}{\partial y} = -gH\frac{\partial \eta^{(1)}}{\partial y}. \tag{28}$$

The forcing from solution 1 appears in the momentum balance equations, rather than in the mass balance as might have been expected. However, by introducing the (approximate) total sea surface uplift,

$$\eta' = \eta^{(1)} + \eta^{(2')}, \tag{29}$$

and eliminating $\eta^{(2')}$ in favour of η', we can replace these equations with

$$\frac{\partial \eta'}{\partial t} + \frac{\partial q_x^{(2')}}{\partial x} + \frac{\partial q_y^{(2')}}{\partial y} = \frac{\partial \eta^{(1)}}{\partial t}, \tag{30}$$

$$\frac{\partial q_x^{(2')}}{\partial t} + gH\frac{\partial \eta'}{\partial x} = 0, \tag{31}$$

$$\frac{\partial q_y^{(2')}}{\partial t} + gH\frac{\partial \eta'}{\partial y} = 0. \tag{32}$$

This formulation matches the one introduced by Saito *et al.* (2019). The forcing has now been transferred to the mass balance, similar to the tsunami problem in the one-way coupled methods 2 and 3.

Finally, we note that the Boussinesq correction terms can be added to the horizontal momentum balances (eqs 31 and 32) to account for dispersion during tsunami propagation. Regardless of the choice of shallow water solver, non-hydrostatic effects during tsunami generation are naturally accounted for in solution 1, by virtue of solving for the ocean response using a depth-resolved solver. This is similar to, but potentially superior to, the use of a Kajiura filter in that solution 1 accounts for the non-hydrostatic response of a variable depth ocean, whereas the Kajiura filter assumes a uniform depth ocean.

2.5 Implementation of the methods

This section explains how the four methods introduced above are implemented and utilized in our study. We use the 3-D dynamic rupture and wave propagation code SeisSol, which solves the elastic and acoustic wave equations in velocity-stress formulation using the arbitrary high-order derivative Discontinuous Galerkin (ADER-DG) method, with kinematic or dynamic rupture sources (Dumbser & Käser 2006; Pelties *et al.* 2014; Uphoff *et al.* 2017; Krenz *et al.* 2021). See A for verification of this new boundary condition and Krenz *et al.* (2021) for discussion of high performance computing aspects of the implementation. We use SeisSol with gravity to provide the method 1 solution, and an otherwise identical solution without gravity to provide the static or time-dependent forcing for methods 2–4. For the shallow water model in methods 2–4, we solve the non-dispersive linear long wave equations using the code FDMAP (Dunham *et al.* 2011; Kozdon *et al.* 2012, 2013). While FDMAP was written for 2-D antiplane shear and plane strain elastodynamic problems, the linear long wave equations are mathematically equivalent to the 2-D antiplane shear wave equation. In one example at the end of our study (Section 6.2), we use a Boussinesq solver that accounts for weak dispersion during tsunami propagation (Saito *et al.* 2010; Saito 2019).

3 SEAFLOOR TO SEA SURFACE TRANSFER FUNCTIONS AND WAVE MODES IN A UNIFORM DEPTH OCEAN

Having presented the four methods, we now compare them. One way to do this is to examine the sea surface response $\eta(x, y, t)$ to an imposed seafloor uplift $b(x, y, t)$. For a uniform depth ocean (i.e. constant H), this can be quantified in terms of the Fourier domain transfer function

$$T(k, \omega) = \frac{\hat{\eta}(k_x, k_y, \omega)}{\hat{b}(k_x, k_y, \omega)}, \tag{33}$$

for horizontal wavenumbers k_x and k_y and angular frequency ω, using the convention

$$\hat{f}(k_x, k_y, \omega) = \int_{-\infty}^{\infty}\int_{-\infty}^{\infty}\int_{-\infty}^{\infty} f(x, y, t) e^{-i(k_x x + k_y y - \omega t)}\, \mathrm{d}x\, \mathrm{d}y\, \mathrm{d}t\,, \tag{34}$$

$$f(x, y, t) = \frac{1}{(2\pi)^3}\int_{-\infty}^{\infty}\int_{-\infty}^{\infty}\int_{-\infty}^{\infty} \hat{f}(k_x, k_y, \omega) \times e^{i(k_x x + k_y y - \omega t)}\, \mathrm{d}k_x\, \mathrm{d}k_y\, \mathrm{d}\omega\,. \tag{35}$$

The translational invariance of the ocean response in the horizontal directions requires that T depend on k_x and k_y only through the radial wavenumber $k = (k_x^2 + k_y^2)^{1/2}$. Practically, (35) allows to analytically compute the sea surface response from seafloor uplift. Thereby, the (spectral) transfer function quantifies the ocean response to seafloor uplift and contains within it information about wave modes in the ocean and how they are excited by seafloor uplift.

The transfer function for the fully coupled method (i.e. solution to the general problem, method 1) is Lotto & Dunham (2015) and Wilson & Ma (2021)

$$T_{gen}(k, \omega) = \frac{1}{\cosh(k^* H) - (gk^*/\omega^2)\sinh(k^* H)}, \tag{36}$$

where

$$k^* = \sqrt{k^2 - \omega^2/c_0^2}. \tag{37}$$

Poles in the transfer function correspond to the acoustic and surface gravity wave modes, which have received extensive discussion in the literature (Levin *et al.* 2009). Briefly, at a given wavenumber k, there are infinitely many solutions ω to the dispersion relation. There is one surface gravity wave mode (indexed as $n = 0$) and an infinite number of acoustic modes (indexed as $n = 1, 2, \ldots$). Fig. 3(a) shows the amplitude of the transfer function, with large amplitude response corresponding to (k, ω) pairs satisfying the dispersion relation for surface gravity wave and acoustic modes. At small horizontal wavenumbers ($kH \ll 1$), the surface gravity wave mode phase and group velocities asymptote to the non-dispersive shallow water wave speed $(gH)^{1/2}$. The acoustic modes exist as propagating (rather than evanescent) modes only at frequencies greater than a cut-off frequency given approximately by

$$\omega_n \approx (n - 1/2)\pi c_0/H, \quad n = 1, 2, \ldots, \tag{38}$$

and at large horizontal wavenumbers ($kH \gg 1$), their phase and group velocities approach (from above and below, respectively) the sound speed c_0. We remark that replacing the rigid seafloor condition with an elastic half-space (Section 5) modifies the wave modes, especially the acoustic modes near their cut-off frequency (Eyov *et al.* 2013). Most importantly, the $n = 1$ mode no longer has a cut-off frequency, and transitions to an oceanic Rayleigh wave (Biot 1952) in the low frequency ($\omega H/c_0 \ll 1$) limit. We explore this in more detail in Section 5.

In the incompressible limit, $k^* \to k$ and the transfer function reduces to

$$T_{inc}(k, \omega) = \frac{1}{\cosh(kH) - (gk/\omega^2)\sinh(kH)}. \tag{39}$$

Surface gravity waves obey the dispersion relation $\omega^2 = gk\tanh(kH)$. Note also that the instantaneous ($\omega \to \infty$) response is the well-known $1/\cosh(kH)$ Kajiura filter (Kajiura 1970). In the long wavelength ($kH \ll 1$) limit, the incompressible transfer function is

$$T_{LLW}(k, \omega) = \frac{1}{1 - gHk^2/\omega^2}. \tag{40}$$

The absence of the $1/\cosh(kH)$ filter means that all wavelengths of seafloor displacements are transferred to the sea surface. Likewise, the surface gravity wave mode propagates non-dispersively at the shallow water speed: $\omega/k = (gH)^{1/2}$ (Fig. 3d, bottom panel). As the linear long wave model (used in methods 2, 3) assumes an incompressible ocean, its transfer function lacks acoustic wave modes (Fig. 3d, top panel).

The linear long wave model can be replaced with the Boussinesq model, which has transfer function

$$T_{Bous}(k, \omega) = \frac{1}{1 - \frac{gHk^2}{\omega^2}\left[1 + \frac{(kH)^2}{3}\right]}. \tag{41}$$

This result follows from the transform-domain solution of eqs (9), (13), and (14). The associated dispersion relation, $\omega^2 = gHk^2[1 + (1/3)(kH)^2/3]^{-1}$, features a leading order dispersive correction to the linear long wave model.

The superposition method (method 4) sequentially solves two problems, using forcing from the first (zero-gravity) problem in the second (shallow water) problem. Its transfer function can therefore be factored as

$$T_{sup}(k, \omega) = T_{g=0}(k, \omega)T_{SW}(k, \omega), \tag{42}$$

in which

$$T_{g=0}(k, \omega) = \frac{1}{\cosh(k^*H)} \tag{43}$$

is obtained by setting $g = 0$ in eq. (36) and T_{SW} is given by either eq. (40) or (41) for the linear long wave and Boussinesq models, respectively. The zero-gravity transfer function (eq. 43) captures the acoustic modes of a compressible ocean bounded by a rigid bottom and free surface, so these modes are expressed in the transfer function for the superposition method (Figs 3b and c, top panels). In addition, in the low frequency limit, or more precisely when horizontal phase velocity is much less than the sound speed [$\omega/(kc_0) \ll 1$], then $k^* \to k$ and the transfer function reduces to the $1/\cosh(kH)$ filter (Kajiura 1970). Thus, the superposition method captures non-hydrostatic ocean response at short wavelengths during the tsunami generation process, even when a linear long wave model is used for tsunami propagation. This is evident in the decreasing amplitude of the transfer function for large kH (Figs 3b and c, bottom panels) in contrast to what is seen for the linear long wave model as used in methods 2 and 3 (Fig. 3d, bottom panel). On the other hand, dispersion is neglected during tsunami propagation when using a non-dispersive linear long wave solver, but is captured (approximately) by using a weakly dispersive Boussinesq solver (compare Figs 3b and c, bottom panels).

4 COMPARING THE FOUR MODELLING METHODS USING AN IMPOSED GAUSSIAN SEAFLOOR DISPLACEMENT

In this section, we perform 3-D numerical simulations to study the wave response of a uniform depth ocean to an imposed seafloor displacement. There is no coupling to an elastic solid. The seafloor uplift rate is a Gaussian in both space and time,

$$\partial b/\partial t = \left(A/(\sigma_t\sqrt{2\pi})\right)\exp\left(-(t - 4\sigma_t)^2/2\sigma_t^2\right) \times \exp\left(-(x^2 + y^2)/2\sigma_r^2\right), \tag{44}$$

where σ_r and σ_t characterize the spatial width and duration of the source and A is amplitude. The maximum uplift rate occurs at time $t = 4\sigma_t$ so that the simulation can begin with effectively zero uplift rate at $t = 0$. We fix $H = 4$ km, $c_0 = 1.5$ km s^{-1} and $g = 9.81$ m s^{-2}, and vary σ_r and σ_t across three scenarios. We set up scenarios to allow for different excitation of tsunami and acoustic waves, showing results for a long duration source, an impulsive source, and an impulsive source with a narrow source width to produce short wavelengths for which we anticipate dispersion and filtering effects in the ocean response (Table 1).

For the three scenarios, domain sizes, discretization, and simulation time varied to best capture important features in the wavefield. The horizontal domain size was large enough to avoid boundary reflections. The element size was set to a uniform characteristic edge length in the interior region of the domain and increased to a larger characteristic length outside this region. For scenario 1, the domain was 500 km by 500 km with an interior region 300 km by 300 km with a characteristic element edge length of 1.5 km and an outer characteristic element length of 75 km; the simulation was run for 800 s. For scenario 2, the domain was 200 km by 200 km with an interior region 110 km by 110 km with a characteristic element length of 1 km and an outer characteristic element length of 75 km; the simulation was run for 400 s. For scenario 3, the domain was 400 km by 400 km with an interior region 40 km by 40 km with a characteristic element edge length of 0.25 km and an outer characteristic element edge length of 25 km; the simulation was run for 150 s.

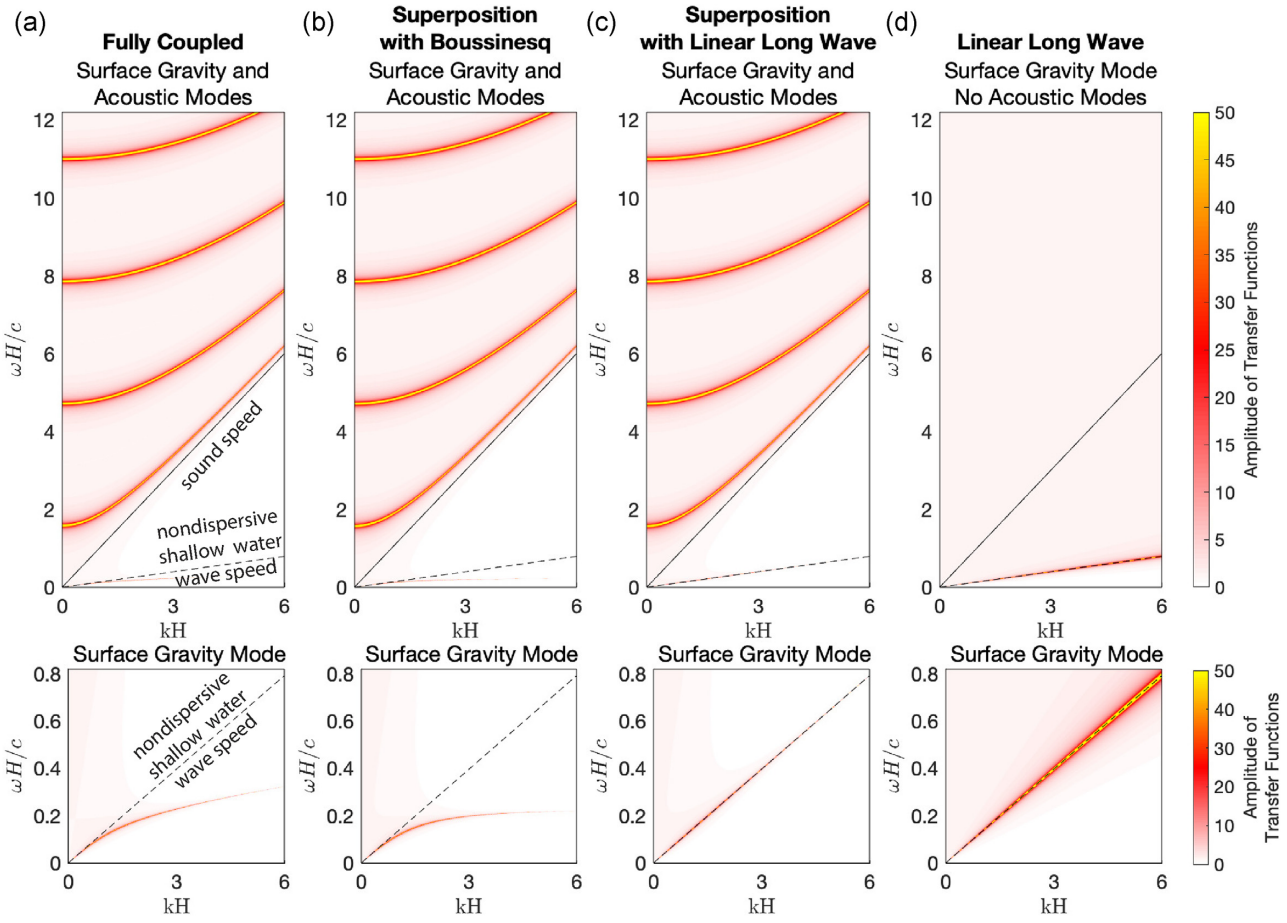

Figure 3. Amplitude of transfer functions for (a) fully coupled model, (b) superposition with Boussinesq model, (c) superposition with linear long wave model and (d) linear long wave model by itself. Top panels show higher values of $\omega H/c$ to highlight acoustic modes, whereas bottom panels focus on the surface gravity wave mode.

Table 1. Three scenarios involving a prescribed seafloor uplift rate that is Gaussian in space and time, with width σ_r and duration σ_t. Three non-dimensional parameters control the solution and validity of the assumptions used in modelling methods 2–4.

	Source width σ_r (km)	Source duration σ_t (s)	Instantaneous source $\sqrt{gH}\sigma_t/\sigma_r \ll 1$	Negligible acoustic wave excitation $H/(c_0\sigma_t) \ll 1$	Shallow water limit $H/\sigma_r \ll 1$
Scenario 1	12.5	125	Violated	Justified	Justified
Scenario 2	12.5	1.25	Justified	Violated	Justified
Scenario 3	1.25	1.25	Justified	Violated	Violated

4.1 Ocean transfer function and source spectrum determine excitation of wave modes

The transfer functions derived previously allow us to anticipate the wave modes that will be excited by the imposed seafloor displacement. Fourier transforming $b(x, y, t)$ using eq. (34) gives

$$\hat{b}(k,\omega) = \frac{A}{-i\omega} 2\pi\sigma_r^2 \exp\left(-\sigma_t^2\omega^2/2 + 4i\sigma_t\omega\right) \exp\left(-\sigma_r^2 k^2/2\right). \tag{45}$$

This source primarily excites waves having angular frequencies below σ_t^{-1} and wavenumbers below σ_r^{-1}. Given the seafloor displacement spectrum $\hat{b}(k, \omega)$, the sea surface spectral response can be calculated using the transfer function as $\hat{\eta}(k, \omega) = T(k, \omega)\hat{b}(k, \omega)$. Fig. 4 shows the imposed seafloor displacement spectrum and the sea surface response for the four modelling methods.

Scenario 1 (Fig. 4, left-hand column) is a long duration source ($\sigma_t = 125$ s). Because $H/(c_0\sigma_t) \ll 1$, the excitation occurs only for angular frequencies satisfying $\omega H/c_0 \ll 1$. Compressibility effects in the ocean are negligible, so only surface gravity waves are generated, in contrast to the shorter duration sources ($\sigma_t = 1.25$ s) in scenarios 2 and 3 (Fig. 4, middle and right-hand columns) that also excite acoustic waves.

Scenarios 2 and 3 differ in the source width σ_r, with the narrow width in scenario 3 leading to pronounced dispersion of the

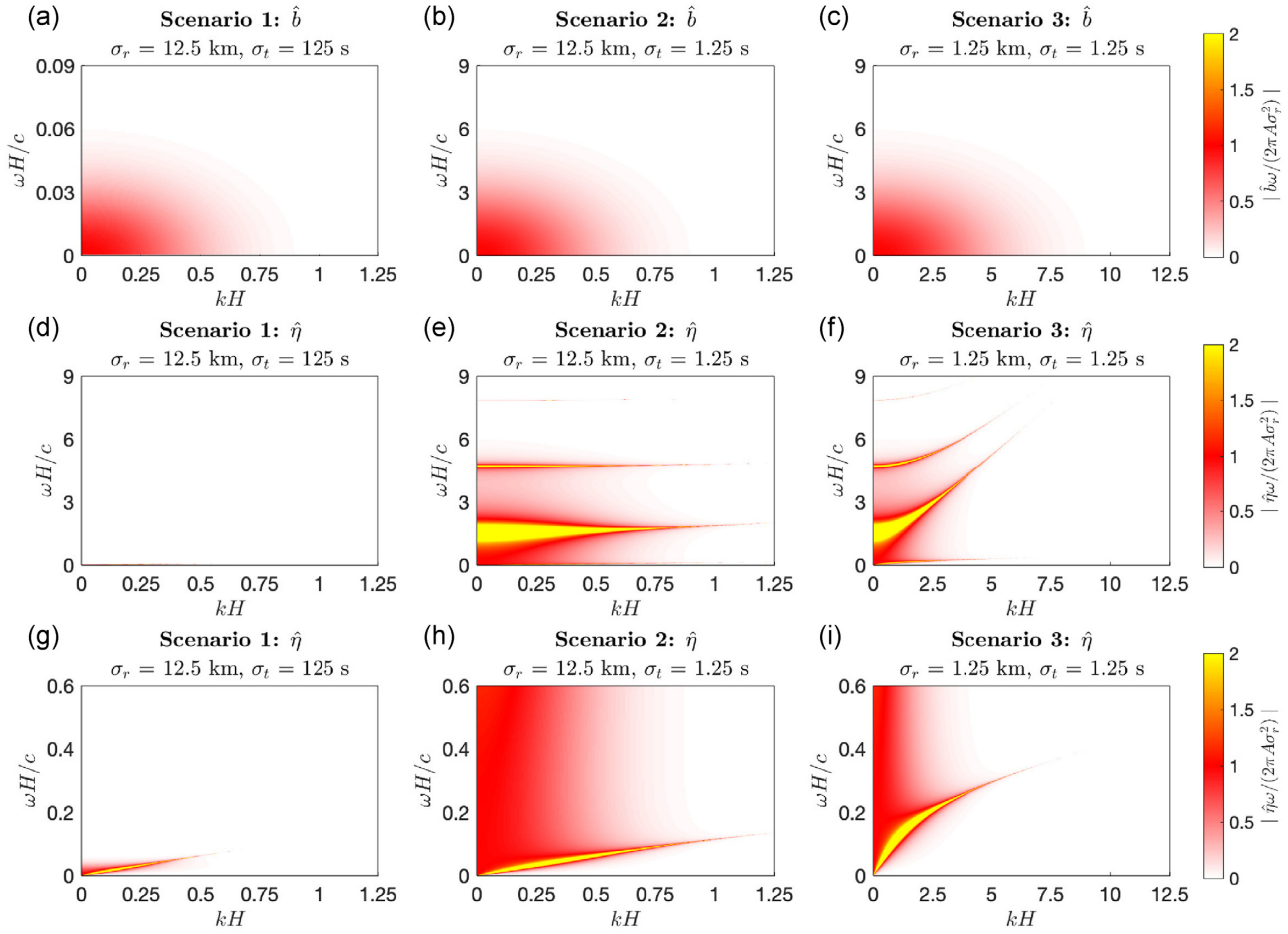

Figure 4. Fourier domain seafloor displacement (a–c) and sea surface response (d–i) for three scenarios having different spatial widths σ_r and durations σ_t of the imposed seafloor displacement. The long duration of scenario 1 prevents excitation of acoustic wave modes, in contrast to the shorter duration scenarios 2 and 3. The long duration also requires accounting for tsunami propagation during the wave generation process. The narrower width of scenario 3 produces dispersion of the surface gravity wave mode.

surface gravity wave mode and the filtering of short wavelengths when translating seafloor displacement to sea surface displacement. The relevant dimensionless parameter determining this behaviour is H/σ_r.

Finally, scenario 1 provides an example of a long duration source for which tsunami propagation occurs during the wave generation process, violating one of the assumptions made for method 2. The importance of this effect can be assessed by comparing the tsunami propagation distance during the earthquake duration, $\sqrt{gH}\sigma_t$, to the spatial extent of the source, σ_r. When $\sqrt{gH}\sigma_t/\sigma_r \ll 1$, then the source is effectively instantaneous; otherwise a time-dependent tsunami source must be considered.

To summarize, we have identified three dimensionless parameters that control the solution behaviour for our Gaussian source, specifically the excitation of acoustic waves $[H/(c_0\sigma_t)]$, shallow water limit (H/σ_r), and whether tsunami propagation will occur over the source duration $(\sqrt{gH}\sigma_t/\sigma_r)$. These dimensionless parameters can be used to determine if the assumptions of modelling methods 2–4 are justified and to anticipate what solution features will be inaccurate when these assumptions are violated.

4.2 Numerical simulations of the ocean response to an imposed Gaussian seafloor displacement

Next we apply the four modelling methods to this problem, using numerical simulations that are implemented as described in Section 2.5. Results are shown in Fig. 5. For this problem, the shallow water solver used in methods 2–4 is the non-dispersive linear long wave model, and we do not apply the Kajiura filter for methods 2 and 3. For the instantaneous source model 2, we set the initial sea surface height to be equal to the seafloor displacement at the end of the earthquake simulation; at this point the seafloor is no longer deforming. We shift the start time of the tsunami to the time at which the Gaussian uplift rate is maximum.

Scenario 1 (Fig. 5, top row) features a wide, long duration source. The ocean responds in the shallow water limit, with negligible filtering of short wavelengths during tsunami generation and dispersion during tsunami propagation. The long duration implies that acoustic wave excitation is negligible and that the tsunami propagates over the source duration. The main feature in all four methods is the tsunami wave propagating with velocity $(gH)^{1/2}$. Methods 1, 3 and 4, which all account for the finite duration of the source, produce

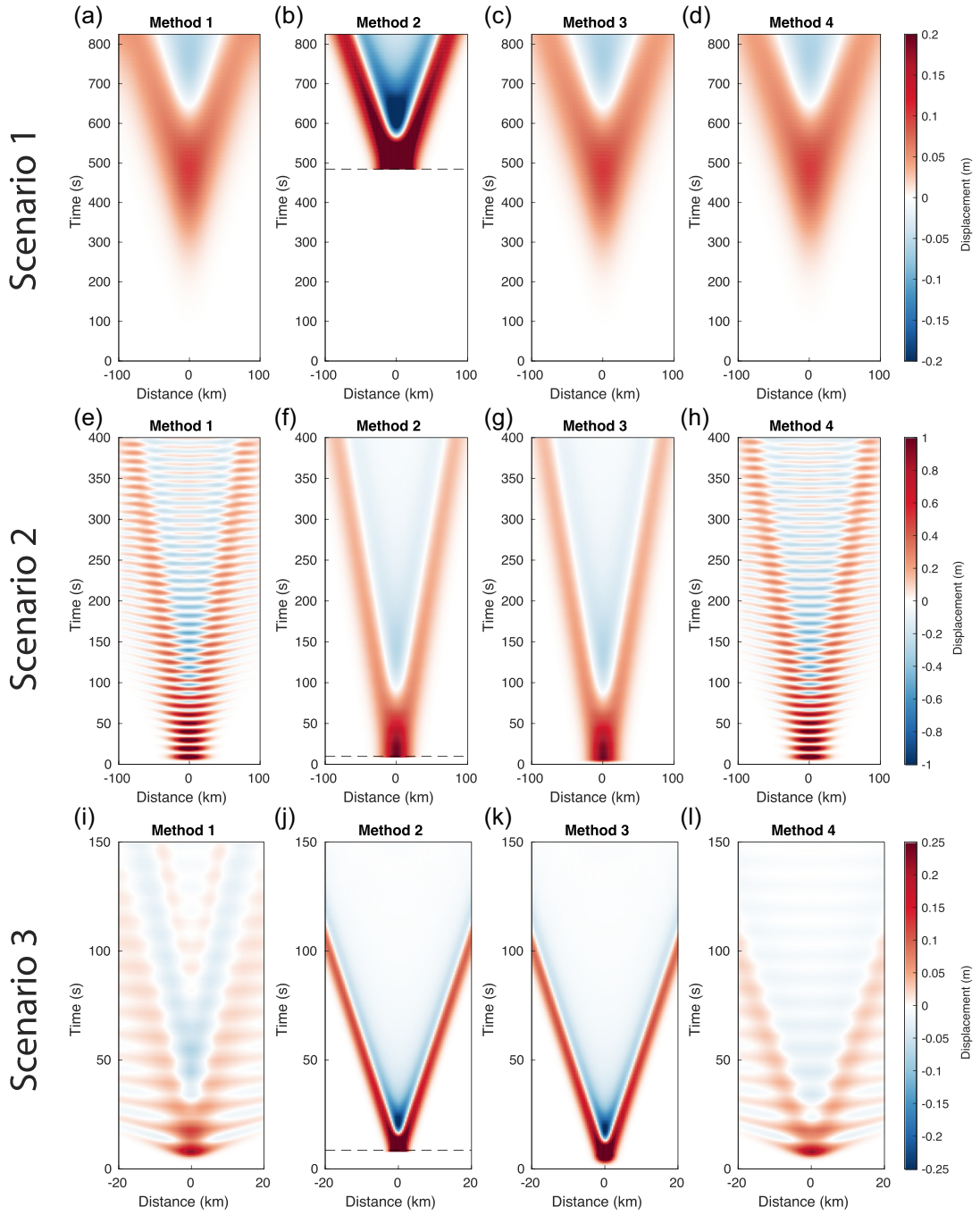

Figure 5. Simulation results of sea surface displacement, plotting along an arbitrary cross-section through the centre of the source, for the three scenarios (panel rows) using the four modelling methods (panel columns). Scenario 1: For this long duration source, tsunami propagation during the wave excitation process leads to reduced amplitudes as compared to the method 2 assumption of an instantaneous source. Negligible acoustic waves are excited. Scenario 2: The shorter source duration excites acoustic waves. Scenario 3: The narrower source violates the shallow water limit, leading to filtering of short wavelength and dispersion of surface gravity waves.

visually identical solutions. The instantaneous source method 2 differs from the other modelling methods; it overpredicts the tsunami amplitude and underpredicts the tsunami period.

Scenario 2 (Fig. 5, middle row) has the same wide source width as scenario 1 and all four methods accurately capture the tsunami, which propagates with negligible dispersion. The source duration is much shorter, explaining why here the instantaneous source method 2 matches the time-dependent source method 3. The shorter duration source excites acoustic waves, which produce a beating pattern in the space–time plots. The long horizontal wavelength of these waves causes them to be almost vertically propagating, with a horizontal phase velocity that exceeds the sound speed. Methods 1 and 4, which capture acoustic waves, show excellent agreement.

Scenario 3 has the same short duration source as scenario 2, such that acoustic waves are excited, but with a narrower source width. The narrow width excites short wavelength surface gravity waves that violate the shallow water condition $kH \ll 1$, leading to dispersion during propagation. This dispersion is captured only

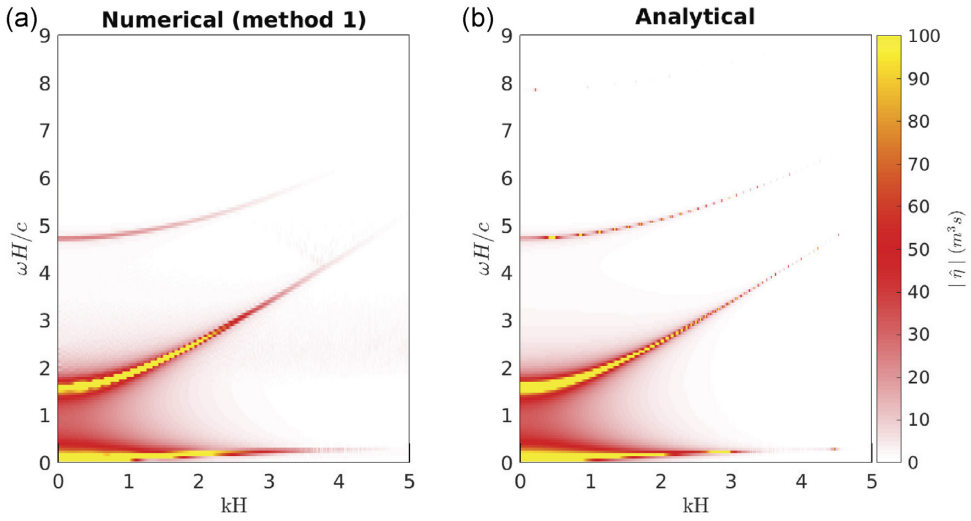

Figure 6. Fourier spectral amplitude of sea surface displacement for scenario 3: (a) method 1 (fully coupled method), computed using FFTs in space and time and (b) analytical solution obtained using the transfer function. The colour scale for spectral amplitude is less saturated than in Fig. 4 in order to more clearly emphasize the very weak excitation of the second acoustic mode as compared to the first acoustic mode.

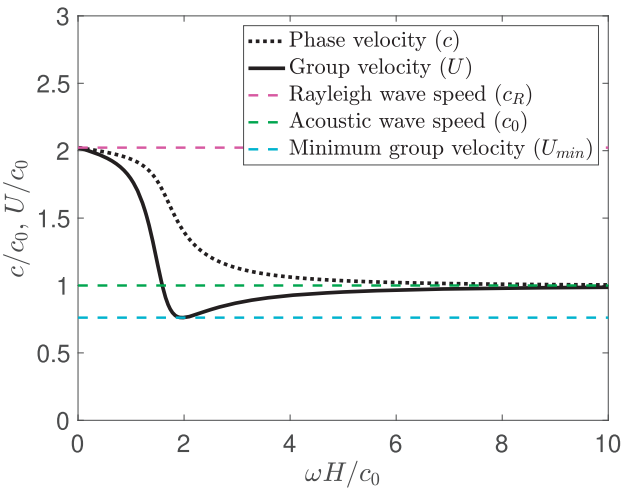

Figure 7. Phase (c) and group velocity (U), normalized by the ocean sound speed c_0, for the $n = 1$ oceanic Rayleigh wave mode as a function of dimensionless angular frequency ($\omega H/c_0$). Also shown as horizontal lines are the Rayleigh wave speed of the solid (c_R), to which both c and U approach as $\omega H/c_0 \to 0$; the ocean acoustic wave speed (c_0); and the minimum group velocity ($U_{\min}$).

in method 1, but not any of the other methods because we use a linear long wave model. The other relevant non-hydrostatic effect is the filtering of short wavelengths in the transfer function between seafloor uplift and sea surface response (Kajiura 1963). This filtering reduces tsunami wave amplitude by over a factor of two in this example and also changes the waveform shape. Method 4 accounts for this filtering effect through the initial zero-gravity simulation that includes a depth-resolved ocean response, even when a non-dispersive linear long wave model is used for tsunami propagation. Thus the tsunami predicted by method 4 agrees much better with that of method 1 than methods 2 and 3, which neglect the filtering effect. The differences between methods 1 and 4 appear only during tsunami propagation, manifesting mainly as dispersion-related features in the trailing edge of the tsunami wave.

Returning to the acoustic waves, we examine which acoustic modes are contributing to the response in scenarios 2 and 3. The transfer function analysis (Fig. 4) shows that the first two acoustic modes should be excited. However, the amplitude of the first acoustic mode is much larger and is expressed over a wider range of frequencies than the second acoustic mode. To confirm this, we perform a spectral analysis (using a discrete Fourier transform in space and time) of the sea surface displacement field from the method 1 numerical solution for scenario 3 and compare this to the analytical solution derived earlier. Results, shown in Fig. 6, show excellent agreement between the numerical and analytical solutions. Thus we conclude that the acoustic wavefield is dominated by the first acoustic mode.

5 EFFECTS OF AN ELASTIC SEAFLOOR ON WAVE MODES

Thus far, we have focused our analysis of wave excitation on an ocean with a seafloor that is rigid, except when prescribing seafloor uplift. Here we extend this analysis by accounting for an elastic half-space underlying the ocean. Our implementation of the fully coupled method in SeisSol permits the simulation of kinematic or dynamic rupture sources with self-consistent excitation of waves in the solid and overlying ocean. While the elasticity of the seafloor has a negligible effect on tsunami generation and propagation, at least for the local and regional scale problems considered in this study, there are pronounced changes to the acoustic response. Specifically, elasticity removes the cut-off frequency of the first acoustic mode, and that mode transitions into a Rayleigh wave as $\omega H/c_0 \to 0$. Hence, there is no clear distinction between seismic and acoustic wave modes in this problem. We examine dispersion properties of this so-called oceanic Rayleigh wave (Biot 1952) and illustrate how the interplay between the frequencies of the source and the frequency at which group velocity has a local minimum determines the expression of this wave mode, specifically the generation of an Airy phase.

An appropriate starting point for our discussion is the dispersion relation for a homogeneous acoustic layer (ocean) of thickness H,

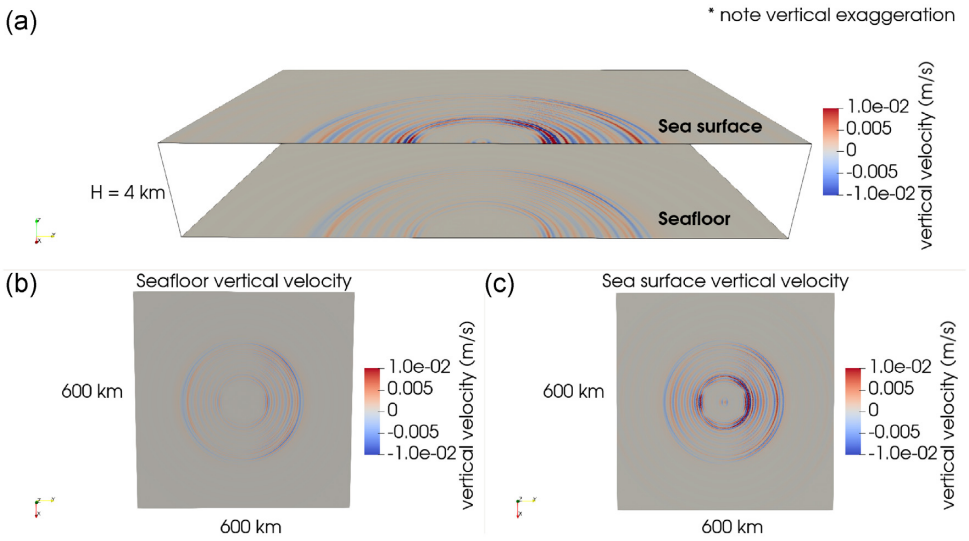

Figure 8. Dynamic rupture on a shallow thrust fault causes the seafloor to deform and the ocean to respond. Shown is the vertical velocity for a fully coupled method simulation for an ocean of depth $H = 4$ km at $t = 120$ s. (a) Half the domain is shown (sliced across strike for ease of visualizing both surfaces), with the seafloor below and sea surface above. (b) Vertical velocity on the seafloor. (c) Vertical velocity on sea surface.

Table 2. Parameter values for dynamic rupture simulations.

Parameter	Symbol	Value
Density in ocean	ρ	1000 kg m^{-3}
Sound speed in ocean	c_0	1500 m s^{-1}
Density in solid	ρ_s	2700 kg m^{-3}
Gravity	g	9.81 m s^{-2}
P-wave speed in solid	c_p	5716 m s^{-1}
S-wave speed in solid	c_s	3300 m s^{-1}
Ocean depth	H	Variable
Fault dip	θ	15°
Fault length along-strike		30 km
Fault length downdip		15 km
Static friction inside nucleation zone	$\mu_{s,\,\mathrm{in}}$	0.57
Static friction outside nucleation zone	$\mu_{s,\,\mathrm{out}}$	0.60
Dynamic friction	μ_d	0.40
Slip-weakening distance	D_c	0.3 m
Cohesion	c	0.15 MPa
Principal total stress ratio	C	1.5
Hubbert–Rubey pore fluid pressure ratio	λ	0.8278

density ρ, and sound speed c_0 over a homogeneous elastic half-space of density ρ_s and *P*- and *S*-wave speeds c_p and c_s. We neglect gravity in this analysis and utilize a standard $p = 0$ free surface condition on the ocean surface, which is appropriate for studying acoustic and seismic waves at frequencies above ∼1 mHz as explained below. Given an angular frequency ω, we solve the dispersion relation for horizontal wavenumbers k. For a sufficiently high frequency there are multiple solutions, indexed by the integer n (and starting at $n = 1$ rather than with the $n = 0$ surface gravity wave mode because gravity is neglected). Here we focus exclusively on the $n = 1$ oceanic Rayleigh wave mode.

To justify neglecting gravity, we start with the free surface boundary condition with gravity. eqs (6) and (7) can be combined in the frequency domain as $\hat{p} = Z_g(\omega)\hat{v}_z$, where $Z_g(\omega) = \rho g/(-i\omega)$ is the impedance of the surface. When Z_g is small compared to the impedance associated with the wave modes of interest, it can be neglected (which corresponds to setting $p = 0$). For acoustic and seismic waves, relevant solutions will have pressure and velocity related by an acoustic or seismic impedance of order density times acoustic or seismic wave speed, for example ρc_0. Therefore, the dimensionless ratio of impedances is of order $g/(-i\omega c_0) \sim (1\ \mathrm{mHz}/f)$. At frequencies $f \sim 0.1$ Hz, the relative error incurred in using $p = 0$ as the top boundary condition is only $\sim 10^{-2}$.

Defining horizontal phase velocity $c = \omega/k$, the dispersion relation is (Biot 1952; Eyov *et al.* 2013)

$$4\alpha_s\alpha_p - \left(1+\alpha_s^2\right)^2 = \frac{\rho c^4}{\rho_s c_s^4}\frac{\alpha_p}{\alpha_0}\tan\left(\frac{\alpha_0\omega H}{c}\right), \tag{46}$$

where

$$\alpha_p = \sqrt{1-\frac{c^2}{c_p^2}}, \quad \alpha_s = \sqrt{1-\frac{c^2}{c_s^2}}, \quad \text{and } \alpha_0 = \sqrt{\frac{c^2}{c_0^2}-1}. \tag{47}$$

The left-hand side of eq. (46) is the Rayleigh function

$$R(c) = 4\alpha_s\alpha_p - \left(1+\alpha_s^2\right)^2, \tag{48}$$

which has a single non-dispersive solution c_R that satisfies $R(c_R) = 0$. When $\omega H/c_0 \to 0$, the right-hand side of eq. (46) also goes to zero. In this limit, the ocean response becomes negligible and the solution approaches the non-dispersive Rayleigh wave in the elastic half-space. In the opposite limit $\omega H/c_0 \to \infty$, the solution becomes a non-dispersive Scholte wave propagating at the elastic-acoustic interface and having velocity only slightly less than c_0 (Biot 1952). Of particular note is that this $n = 1$ mode exists for all frequencies, in contrast to the case of a compressible ocean with a rigid bottom. Like the rigid-bottom case, the elastic-bottom case has higher mode solutions that exist only above a cut-off frequency (Biot 1952; Eyov *et al.* 2013). These higher modes are not appreciably excited in our simulations due to the smoothness of the source.

Fig. 7 shows the phase velocity ($c = \omega/k$) and group velocity ($U = \mathrm{d}\omega/\mathrm{d}k$) for the $n = 1$ oceanic Rayleigh wave mode. The group velocity reaches a minimum, $U_{\min}$, at a frequency $f_{\min}$ that is slightly greater than the cut-off frequency of the $n = 1$ mode for a rigid-bottom ocean ($f = c_0/(4H)$ or $\omega H/c_0 = \pi/2$), reflecting a resonance

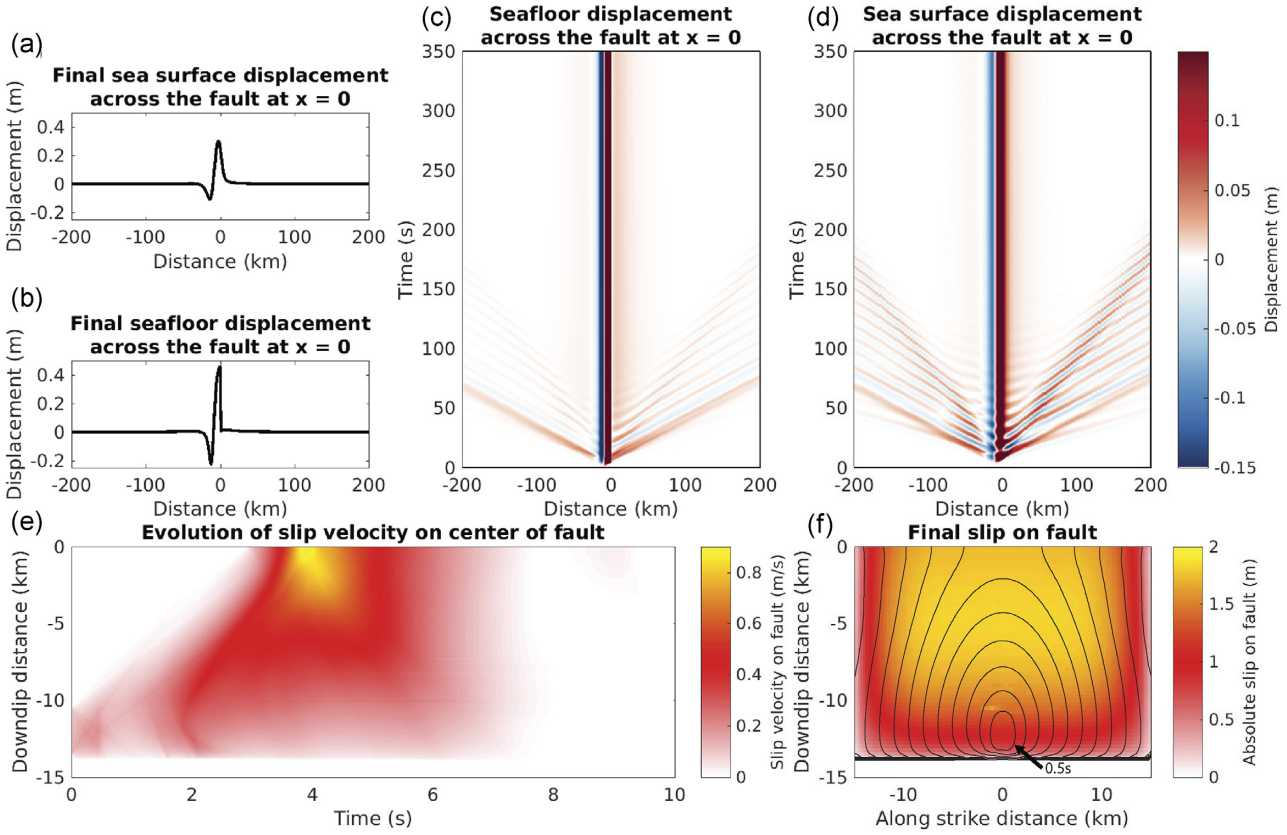

Figure 9. Dynamic rupture simulation with ocean depth $H = 4$ km and no gravity. Space-time plots of (c) seafloor and (d) sea surface vertical displacement along a cross-section perpendicular to strike through the centre of the fault, with static displacements (at $t = 350$ s) shown in (a) and (b). (e) Space-time plot of slip velocity along a cross-section extending downdip through the centre of the fault. (f) Final slip on fault with 0.5 s rupture front contours.

condition within the ocean. The minimum group velocity is less than the ocean sound speed ($U_{\min} < c_0$). Normal dispersion ($\mathrm{d}U/\mathrm{d}\omega < 0$) occurs for frequencies lower than the minimum in group velocity. Anomalous dispersion ($\mathrm{d}U/\mathrm{d}\omega > 0$) occurs at higher frequencies.

The structure of the dispersion curve controls the expression of oceanic Rayleigh waves from an earthquake source, as we demonstrate with numerical simulations in the following section. However, following (Aki & Richards 2002, ch. 7.1), we can anticipate key features of the wavefield. Consider the response at fixed horizontal distance r away from the source. The initial oceanic Rayleigh wave arrivals, appearing at time $t = r/c_R$, have the lowest frequencies. The dominant frequency then increases with time as normally dispersed waves with slower group velocities arrive. This continues until approximately $t = r/c_0$, at which time there exist two solutions to the dispersion relation having identical group velocities. One solution (with normal dispersion) continues the increasing frequency trend seen earlier, while the second (with anomalous dispersion) appears at a much higher frequency that decreases with time. This superposition of normally and anomalously dispersed waves continues until the arrival of the Airy phase at $t = r/U_{\min}$. The relative amplitude of the normally and anomalously dispersed waves depends, in part, on the source spectrum. In particular, the wavefield of a source that excites no waves above the frequency of minimum group velocity $f_{\min}$ will lack the anomalously dispersed waves and Airy phase. This condition can be met by a low frequency source spectrum or by having a sufficiently shallow ocean.

6 DYNAMIC RUPTURE SIMULATIONS AND OCEANIC RAYLEIGH WAVES

In this section we complement our previous numerical simulations of the ocean response to an imposed Gaussian-shaped seafloor uplift with dynamic rupture simulations in a coupled ocean-solid Earth material structure (Fig. 8). Specifically, we compare the four modelling methods with a dynamic rupture source and varying water depth to show the effect of water depth on the excitation and propagation of the tsunami, acoustic, and seismic waves. We use only the linear long wave model for tsunami propagation in methods 2 and 3, but we use both linear long wave and Boussinesq models for method 4 to illustrate the importance of accounting for dispersive tsunami propagation.

6.1 Problem setup

The dynamic rupture simulation is conducted for a low angle thrust fault in a homogeneous elastic half-space overlain by a compressible ocean of uniform depth H. The x-axis follows the strike of the fault with y being the other horizontal direction perpendicular to strike (with the fault dipping in the $-y$ direction) and z being vertical (positive up with $z = 0$ at the seafloor). Parameter values are given in Table 2. The planar rectangular fault having along-strike length of 30 km dips 15° with respect to the seafloor. Initial stress conditions assume pore fluid overpressure with effective principal

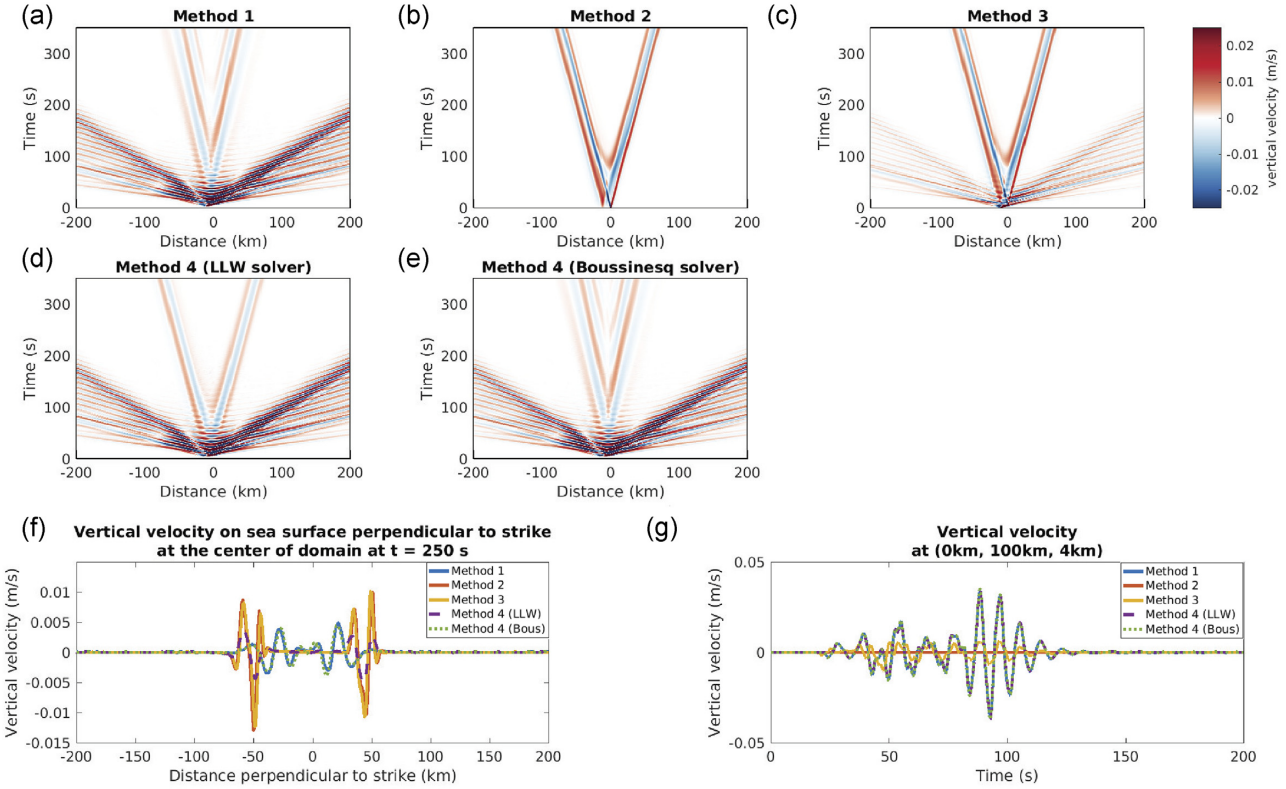

Figure 10. (a–e) Sea surface vertical velocity along a cross-section perpendicular to strike through the centre of the fault for the four modelling methods with an ocean depth of $H = 4$ km. (a) Method 1 (fully coupled method), (b) Method 2 (instantaneous source method), (c) Method 3 (time-dependent source method), (d) Method 4 with a linear long wave (LLW) solver (superposition method) and (e) Method 4 with a Boussinesq (Bous) solver (superposition method). While both variants of method 4 account for non-hydrostatic filtering effects during tsunami generation, only the Boussinesq model accurately captures dispersion during tsunami propagation. (f) Tsunami wave highlighted at single time $t = 250$ s, on the sea surface perpendicular to strike at the centre of the domain and (g) Seismic/acoustic wave highlighted at a single receiver located on the sea surface at $x = 0, y = 100$ km.

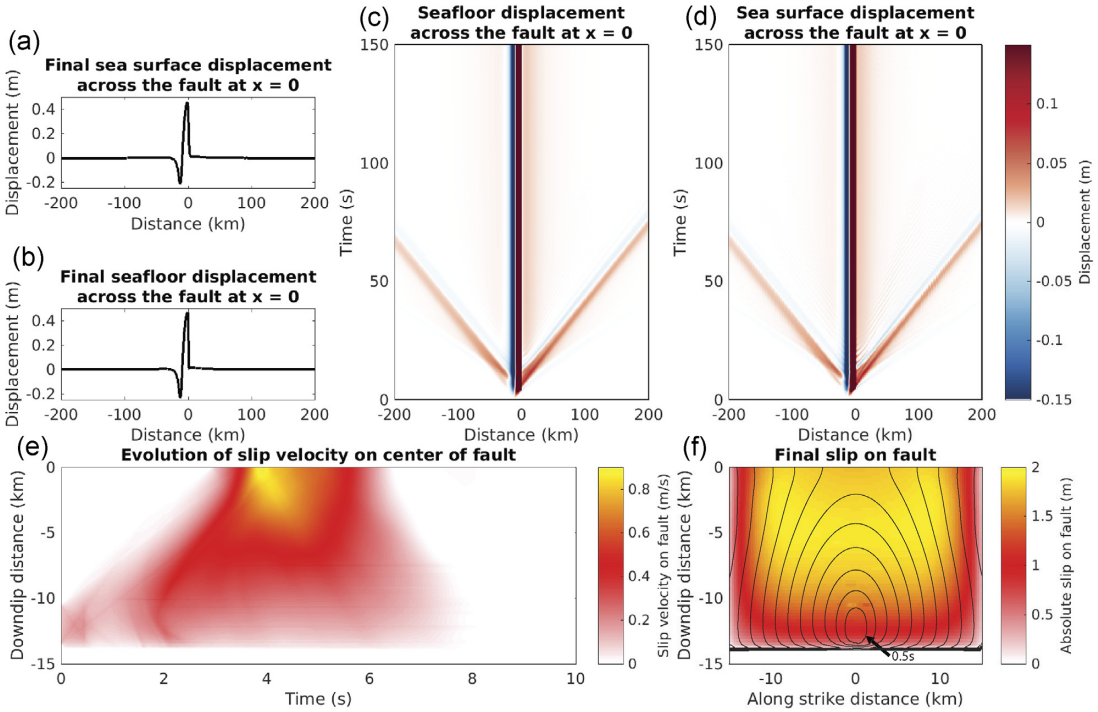

Figure 11. Same as Fig. 9 except for $H = 1$ km.

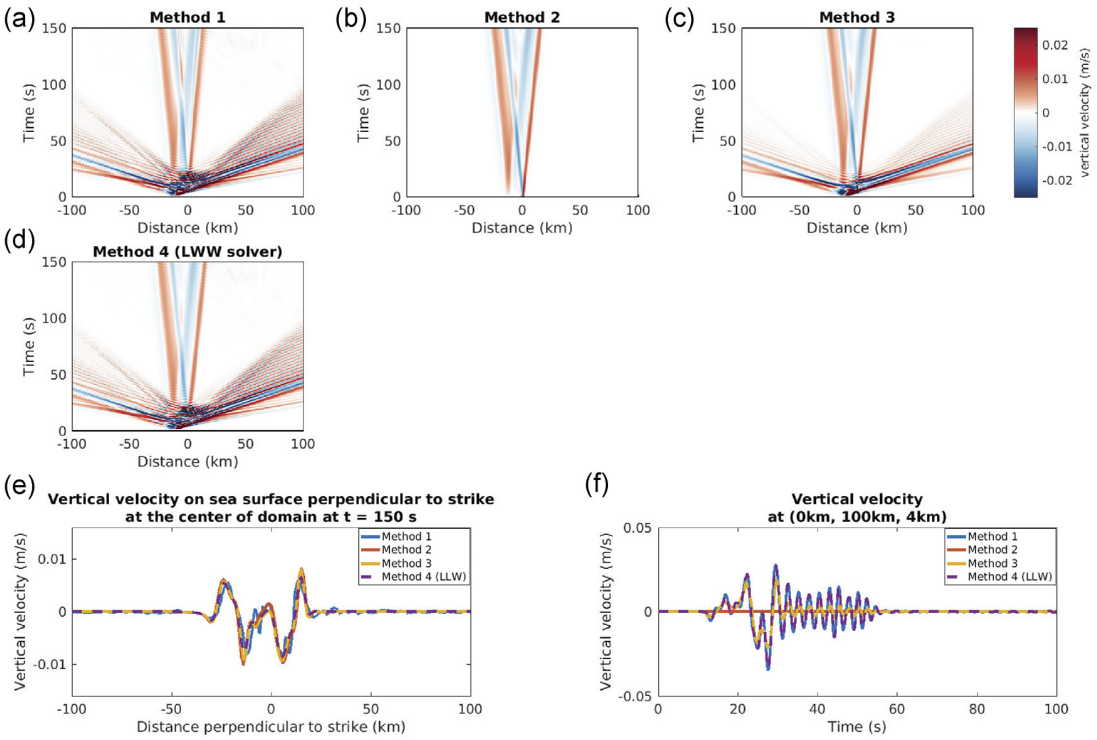

Figure 12. Same as Fig. 10 except for $H = 1$ km.

stresses increasing linearly with depth as

$$\sigma'_{yy}(z) = (C - \lambda)\rho_s g z, \quad \sigma'_{zz}(z) = (1 - \lambda)\rho_s g z, \tag{49}$$

and $\sigma'_{xx} = (\sigma'_{yy} + \sigma'_{zz})/2$. We choose the constant principal total stress ratio $C = 1.5$ and the Hubbert–Rubey pore fluid pressure ratio $\lambda = \rho/\rho_s + 0.4574$ to produce a reasonable stress drop after selecting friction parameters. The ratio of horizontal to vertical effective stresses is $(C - \lambda)/(1 - \lambda) = 3.9031$. Below a downdip distance of 13.8 km, all principal stresses are set to lithostatic to arrest the rupture and limit the downdip extent of slip. The simulations are set up to allow for overpressured portion of the fault to slip once nucleated, here we specifically set up simulations to have the fault to slip to the surface.

We use linear slip-weakening friction with cohesion. The rupture is initiated by reducing the static friction coefficient in a square nucleation zone having length and width of 3 km, centred 12 km downdip, so that the prescribed initial stress exceeds peak strength in this region at the start of the simulation (Harris *et al.* 2011, 2018).

The computational domain has an acoustic ocean (of depth $H =$ 4 km) above a 220 km deep elastic Earth, stretching 1200 km in both horizontal directions, with absorbing boundary conditions on the sides and bottom boundaries. We use an unstructured tetrahedral mesh. The element size increases from 100 m around the fault nucleation zone to 250 m on the edges of the fault. Away from the fault, the element size increases gradually to 7.5 km.

For modelling methods requiring a separate tsunami simulation, the solution is interpolated onto a Cartesian mesh. This is then used as input for the tsunami model. For the linear long wave tsunami solver (FDMAP), we divided the 600 km by 600 km domain into an interior region of 400 km by 400 km with 1 km grid spacing and outer region in which grid spacing increases to 10 km. For the Boussinesq tsunami solver, the 400 km by 400 km domain has a uniform 1 km grid spacing.

6.2 Comparison of modelling methods

Fig. 9 shows the rupture history and seafloor and sea surface displacements from a simulation with no gravity and $H = 4$ km. Rupture propagates updip, exciting oceanic Rayleigh waves and leaving a static displacement of both the seafloor and sea surface. Method 2 uses the final static seafloor displacement at 350 s (Fig. 9b) as the tsunami initial condition. Method 3 uses forcing from the seafloor velocity (Fig. 9c). Method 4 uses forcing from the sea surface velocity (Fig. 9d). The rupture process and seafloor displacements are similar, though not identical, for other ocean depths, confirming the relatively small feedback from the ocean onto the fault that was noted by Kozdon & Dunham (2013).

Fig. 10 shows the vertical sea surface velocity for the four modelling methods for $H = 4$ km. Examining tsunami generation and propagation in the four methods, we see differences in amplitude and waveform shape. Methods 2 and 3 (Figs 10b, c and f) overpredict the tsunami wave amplitude by a factor of two because the non-hydrostatic filtering effect of the ocean is neglected in the tsunami generation process when translating between the seafloor and sea surface. This discrepancy can be reduced using a Kajiura filter, which we have not applied in these examples. Method 4 captures the filtering effect during tsunami generation, so tsunami amplitudes are more consistent with method 1. Whereas we use only the non-dispersive linear long wave model for tsunami propagation in methods 2 and 3, we compare two versions of method 4, one that uses the linear long wave model (Fig. 10d) and a second that uses the weakly dispersive Boussinesq model

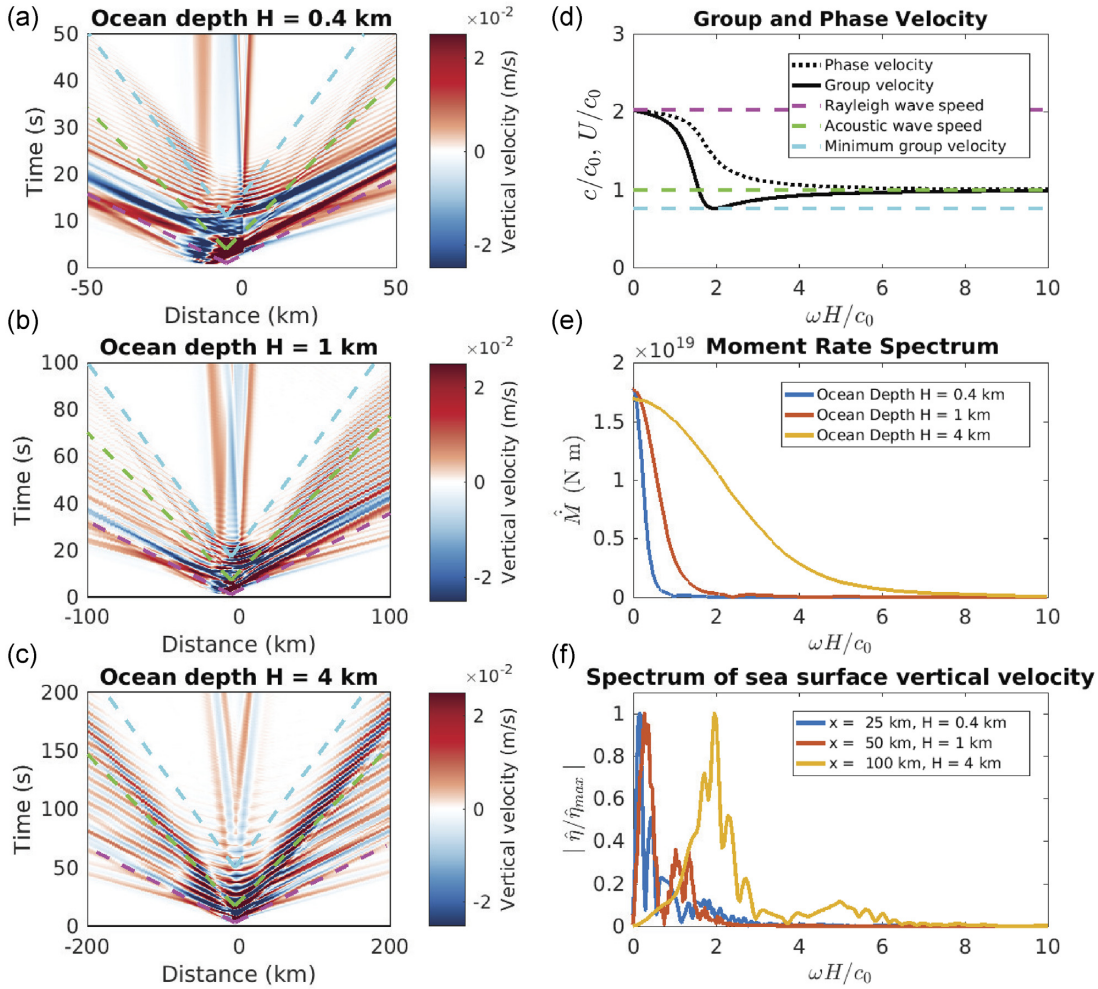

Figure 13. Space-time plots of sea surface vertical velocity showing oceanic Rayleigh waves for ocean depths $H = 0.4$ km (a), $H = 1$ km (b) and $H = 4$ km (c) using the fully coupled method 4. Note different axes limits in (a), (b) and (c). (d) Phase (c) and group velocity (U), normalized by the ocean sound speed c_0 for the oceanic Rayleigh wave mode. (e) Moment rate spectrum of dynamic rupture source. (f) Spectrum of vertical velocity on the sea surface, normalized by maximum amplitude to facilitate comparison.

(Fig. 10d). While the initial tsunami is similar in these two versions of method 4, the tsunami waveform becomes increasingly dissimilar as time progresses (Fig. 10f). The Boussinesq model shows the best agreement with method 1, while the linear long wave model incorrectly predicts a much larger initial wave that arrives too early.

Fig. 10(g) compares seismic and acoustic wave propagation. Seismic and acoustic waves are absent for method 2, which uses the final seafloor displacement as an initial condition for the tsunami simulation. Methods 1, 3 and 4 all feature seismic and acoustic waves, with the largest amplitude waves being oceanic Rayleigh waves that show enhanced amplitudes in the $+y$ direction of updip rupture propagation (Figs 10a–e). Both methods 3 and 4 use time-dependent forcing that includes seismic/acoustic waves from the zero gravity simulation, but method 3 uses forcing from the seafloor and method 4 from the sea surface. This causes method 3 to have an incorrect amplitude for the seismic/acoustic waves (Fig. 10c). This is also evident in a seismogram for a single receiver on the sea surface at $x = 0$, $y = 100$ km (Fig. 10g). We note that some implementations of method 3 filter the seafloor displacement to eliminate these acoustic/seismic waves (Madden *et al.* 2021; Aniko Wirp *et al.* 2021) to focus exclusively on the tsunami. In contrast, method 4 produces nearly identical seismic/acoustic waves to method 1. Slight differences may be caused by the lack of restoring force from gravity on the acoustic waves. Negligible differences in the acoustic waves are seen between the linear long wave and Boussinesq versions of method 4.

We repeated this scenario for shallower depth oceans ($H = 0.4$ km and $H = 1$ km). Results for $H = 1$ km are shown in Figs 11 and 12. While the rupture histories are similar to the $H = 4$ km case, seismic and acoustic waves become less pronounced as H is decreased. In the next section we explain how H influences the seismic/acoustic wavefield.

6.3 Source spectrum and ocean depth control expression of oceanic Rayleigh waves

Our simulations feature prominent oceanic Rayleigh waves, which are the generalization of acoustic waves modes in a rigid-bottomed ocean when accounting for the elasticity of the solid. Ocean depth H alters the dispersion properties of oceanic Rayleigh waves, in

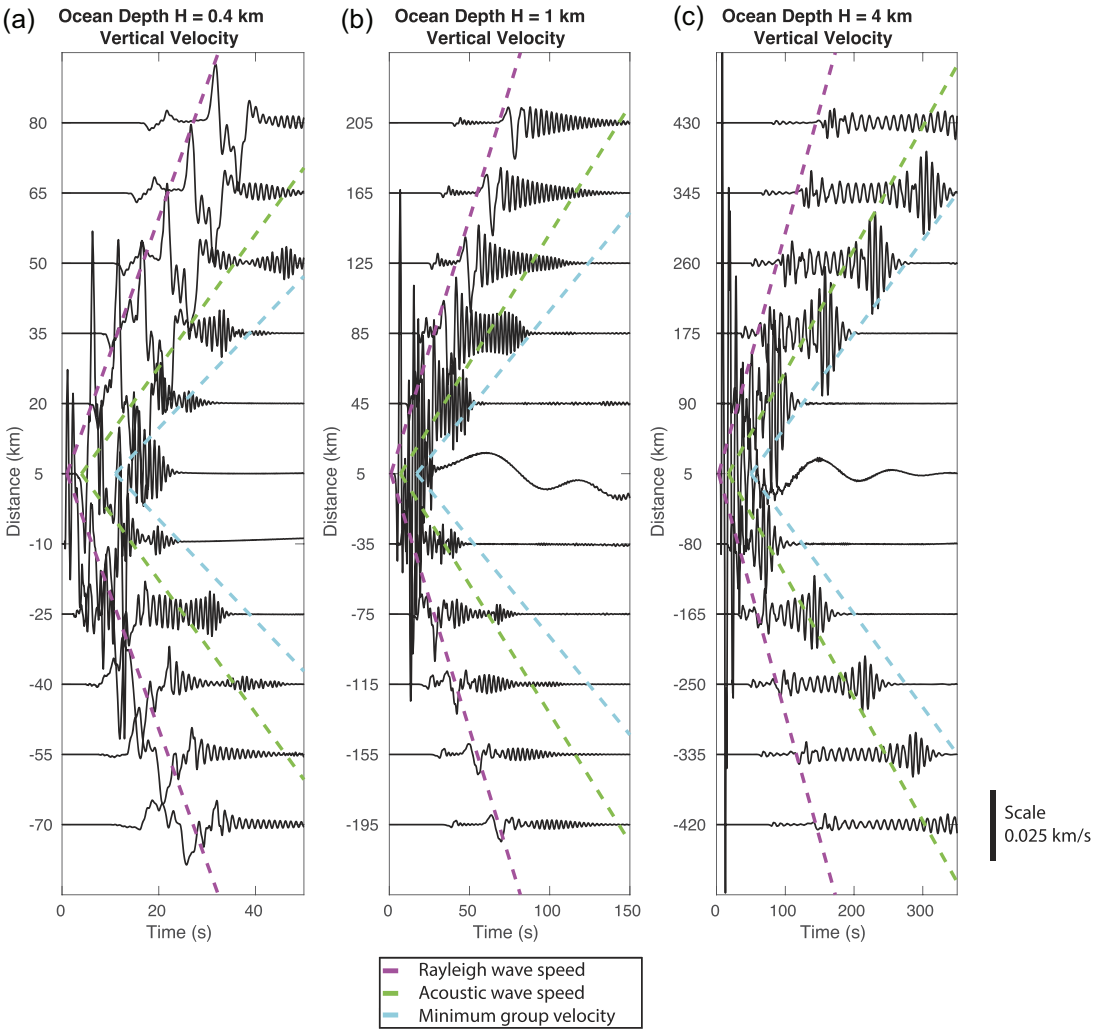

Figure 14. Time-series plots of sea surface vertical velocity showing oceanic Rayleigh waves for ocean depths $H = 0.4$ km (a), $H = 0.4$ km (b) and $H = 4$ km (c) using the fully coupled method 4. Note different axes limits in (a), (b) and (c).

particular the frequency $f_{\min}$ at which the group velocity has a minimum $U_{\min}$. The dynamic rupture excites frequencies below some maximum frequency, which we find is approximately independent of ocean depth (because the ocean has only a small influence on the dynamic rupture process). We explain how the character of the oceanic Rayleigh waves changes with ocean depth.

Fig. 13 shows space-time plots of sea surface vertical velocity from the fully coupled method 1 for ocean depths of $H = 0.4$ km, 1 km, and 4 km, along with lines showing the Rayleigh wave speed of the solid c_R, ocean sound speed c_0, and minimum group velocity $U_{\min}$ (see also the dispersion curve in Fig. 7, which is repeated in Fig. 13d). Also shown are moment rate spectra of the ruptures, which help to quantify the frequency content of waves excited by the source. However, for a finite source the radiated wave spectra vary with direction due to directivity effects, so we also plot spectra of sea surface velocity at a point in the forward direction. We also provide time-series of vertical velocity at increasing distances from the fault in Fig. 14. The initial arrivals are PL waves (Kozdon & Dunham 2014; Wilson & Ma 2021), which are followed by a larger amplitude, dispersed wave packet of oceanic Rayleigh waves.

The leading edge of this wave packet propagates at speed c_R, and arrives immediately after it exhibits normal dispersion. These correspond to the normally dispersed branch of the dispersion curve at frequencies less than $f_{\min}$. Amplitudes are largest at the leading edge of this wave packet for the shallow water ($H = 0.4$ km and $H = 1$ km) cases. In contrast, the deep water ($H = 4$ km) case has an additional, larger amplitude set of waves whose leading edge propagates a bit slower than c_0. These correspond to the anomalously dispersed branch on the dispersion curve at frequencies greater than $f_{\min}$. The wave packet terminates with the Airy phase. The anomalously dispersed waves and Airy phase are not seen in the $H = 0.4$ km and $H = 1$ km cases because $f_{\min}$ is larger than the maximum source frequency. Thus we conclude that the source spectrum, together with the ocean depth, determines the expression of the oceanic Rayleigh wave mode that dominates the seismic/acoustic wavefield.

The results shown here help explain features in previous dynamic rupture simulations and in observations. Simulations of the 2011 Tohoku-Oki earthquake by Kozdon & Dunham (2014) revealed a complex wavefield within the ocean, as might be recorded by ocean bottom seismometers and/or pressure sensors. The oceanic Rayleigh wave is a prominent feature in these simulations. The deep ocean in the Japan Trench (reaching 7 km at the trench) leads to the expression of both normally and anomalously dispersed branches of the oceanic

Rayleigh wave, with the largest amplitude waves propagating slower than the ocean sound speed. Similar waveform features are seen in simulations by Wilson & Ma (2021) using the structural model for Cascadia developed by Lotto *et al.* (2018), despite the ocean only reaching about 3 km depth. Wilson & Ma (2021) demonstrate how excitation of oceanic Rayleigh waves depends on shallow rupture behaviour, in particular whether or not rupture occurs via localized slip on the megathrust or transitions to distributed inelastic yielding of sediments.

Oceanic Rayleigh waves, which have long been recognized in seismology (Press *et al.* 1950), have also been observed in both recorded data and 3-D wave propagation simulations. In their study of an earthquake offshore Japan, Nakamura *et al.* (2012) identify large amplitude arrivals in K-NET seismograms along the coast that they attribute to the oceanic Rayleigh waves through 3-D wave propagation simulations and dispersion analysis. Similar results were obtained by Sugioka *et al.* (2012) for very low frequency earthquakes offshore in the Nankai Trough. Todoriki *et al.* (2016) further confirmed this interpretation by performing more idealized simulations with uniform depth oceans in addition to modelling waveforms from two earthquakes offshore Japan. Their synthetic seismograms show the same water depth dependence that we have identified in our simulations, with the anomalously dispersed branch and Airy phase being suppressed for sufficiently shallow water. Takemura *et al.* (2018) has extended this work by focusing on complexities created by the low velocity accretionary prism in the Nankai Trough, and Noguchi *et al.* (2016) have studied the conversion of oceanic Rayleigh waves to continental Rayleigh waves as the waves approach land. While these studies utilized seismograms on land, other studies have identified similar dispersed waveform features in ambient noise Green's functions from ocean bottom seismometer data (Takeo *et al.* 2014; Takagi *et al.* 2021).

7 CONCLUSION

In this study, we utilized the Lotto & Dunham (2015) method for coupled earthquake and tsunami simulations, which was recently implemented in the 3-D code SeisSol (Krenz *et al.* 2021). We verified this implementation by performing convergence tests against an analytical eigenmode solution in the Appendix. We then compared the fully coupled method (method 1) with two commonly used tsunami modelling methods (methods 2 and 3) that utilize static or time-dependent seafloor displacement from a previously conducted earthquake simulation. In addition, we investigated an additional method (method 4), introduced by Saito *et al.* (2019), that also involves separate earthquake and tsunami simulations but combines them to provide an approximation to the full seismic, acoustic, and tsunami wavefield. Starting from the governing equations for the fully coupled method, we showed how the other methods can be derived by using various approximations. In particular, this establishes the formal basis for the superposition method 4 and explains why it provides an accurate approximation of the fully coupled solution for most problems of interest in coupled earthquake-tsunami modelling. We also identified dimensionless parameters that can be used to determine if the assumption underlying one of the approximate methods is justified and we provided numerical simulations to support our analysis. To compare the methods, we first studied the ocean response to an imposed seafloor displacement. This was done analytically, using seafloor-to-sea surface transfer functions that quantify how seafloor uplift excites different wave modes within the ocean, and using numerical simulations. We then extended the comparison to a dynamic rupture model with an elastic solid underlying the ocean. The presence of the elastic solid alters the structure and dispersion properties of wave modes in the system. The first acoustic mode in the rigid-bottomed case, which exists only above a cut-off frequency, becomes an oceanic Rayleigh wave that exists at all frequencies. The dispersion properties of the oceanic Rayleigh wave, together with the source spectrum, control the wavefield expression of the earthquake source. Our work can help guide future modelling and data interpretation efforts for offshore earthquakes and tsunamis, especially when working with data from ocean-bottom instruments.

ACKNOWLEDGMENTS

LSA was supported by National Science Foundation Graduate Research Fellowship DGE-1656518, Stanford's Enhancing Diversity in Graduate Education (EDGE) Doctoral Fellowship Program and Diversifying Academia and Recruiting Excellence (DARE) Doctoral Fellowship Program. LK and A-AG acknowledge funding from the European Union's Horizon 2020 Research and Innovation Programme under grant agreement No. 823844 (ChEESE – Centre of Excellence in Solid Earth) and the German Research Foundation (DFG) project BA3529/6-1;GA2465/3-1 (CoCoReCS). A-AG was supported by the European Union's Horizon 2020 research and innovation programme under ERC Starting grant no. 852992 (TEAR), the National Science Foundation (NSF) project EAR-2121568 and Horizon Europe (DT-Geo, grant agreement no. 101058129; Geo-Inquire, grant agreement no. 101058518). The authors gratefully acknowledge the Gauss Centre for Supercomputing e.V. (www.gauss-centre.eu) for providing computing time on the GCS Supercomputer SuperMUC-NG at Leibniz Supercomputing Centre (www.lrz.de, through project pn68fi).

DATA AVAILABILITY

Numerical simulations were performed using SeisSol (https://github.com/SeisSol/SeisSol.git) for 3-D fully coupled simulations, FDMAP (https://bitbucket.org/ericmdunham/fdmap) for 2-D linear long wave simulations, and the code developed by Saito *et al.* (2010) and Saito (2019) for 2-D Boussinesq simulations. Simulation setup files are available at doi:10.25740/jv404dc0795 (https://purl.stanford.edu/jv404dc0795).

REFERENCES

Aki, K. & Richards, P., 2002. *Quantitative Seismology, Geology Seismology,* University Science Books.

Amlani, F. *et al.*, 2022. Supershear shock front contribution to the tsunami from the 2018 Mw 7.5 Palu, Indonesia earthquake, *Geophys. J. Int.,* **230**(3), 2089–2097.

Aniko Wirp, S., Gabriel, A.-A., Schmeller, M., H Madden, E., van Zelst, I., Krenz, L., van Dinther, Y. & Rannabauer, L., 2021. 3D linked subduction, dynamic rupture, tsunami, and inundation modeling: dynamic effects of supershear and tsunami earthquakes, hypocenter location, and shallow fault slip, *Front. Earth Sci.,* **9,** doi:10.3389/feart.2021.626844.

Baba, T. *et al.*, 2016. Large-scale, high-speed tsunami prediction for the Great Nankai Trough Earthquake on the K computer, *Int. J. High Perform. Comput. Appl.,* **30**(1), 71–84.

Baba, T., Allgeyer, S., Hossen, J., Cummins, P.R., Tsushima, H., Imai, K., Yamashita, K. & Kato, T., 2017. Accurate numerical simulation of the far-field tsunami caused by the 2011 Tohoku earthquake, including the

effects of Boussinesq dispersion, seawater density stratification, elastic loading, and gravitational potential change, *Ocean Modell.,* **111,** 46–54.

Baba, T., Takahashi, N., Kaneda, Y., Ando, K., Matsuoka, D. & Kato, T., 2015. Parallel implementation of dispersive tsunami wave modeling with a nesting algorithm for the 2011 Tohoku tsunami, *Pure appl. Geophys.,* **172**(12), 3455–3472.

Bernard, E. & Titov, V., 2015. Evolution of tsunami warning systems and products, *Phil. Trans. R. Soc. A,* **373**(2053), doi:10.1098/rsta.2014.0371.

Biot, M.A., 1952. The interaction of Rayleigh and Stoneley waves in the ocean bottom, *Bull. seism. Soc. Am.,* **42**(1), 81–93.

Breuer, A., Heinecke, A., Rannabauer, L. & Bader, M., 2015. High-order ADER-DG minimizes energy- and time-to-solution of seissol, in *High Performance Computing,* pp. 340–357, Springer International Publishing.

Cheung, K.F., Lay, T., Sun, L. & Yamazaki, Y., 2022. Tsunami size variability with rupture depth, *Nat. Geosci.,* **15**(1), 33–36.

Comer, R.P., 1984. Tsunami generation: a comparison of traditional and normal mode approaches, *Geophys. J. Int.,* **77**(1), 29–41.

Dahlen, F. & Tromp, J., 1999. *Theoretical Global Seismology,* Princeton Univ. Press.

DeDontney, N. & Rice, J.R., 2012. Tsunami wave analysis and possibility of splay fault rupture during the 2004 Indian Ocean earthquake, *Pure appl. Geophys.,* **169**(10), 1707–1735.

Du, Y., Ma, S., Kubota, T. & Saito, T., 2021. Impulsive tsunami and large runup along the Sanriku coast of Japan produced by an inelastic wedge deformation model, *J. geophys. Res.,* **126**(8), e2021JB022098, doi:10.1029/2021JB022098.

Duffy, D.G., 1992. On the generation of oceanic surface waves by underwater volcanic explosions, *J. Volc. Geotherm. Res.,* **50**(3), 323–344.

Dumbser, M. & Käser, M., 2006. An arbitrary high-order discontinuous Galerkin method for elastic waves on unstructured meshes—II. The three-dimensional isotropic case, *Geophys. J. Int.,* **167**(1), 319–336.

Dunham, E.M., Belanger, D., Cong, L. & Kozdon, J.E., 2011. Earthquake ruptures with strongly rate-weakening friction and off-fault plasticity, part 1: planar faults, *Bull. seism. Soc. Am.,* **101**(5), 2296–2307.

Elbanna, A., Abdelmeguid, M., Ma, X., Amlani, F., Bhat, H.S., Synolakis, C. & Rosakis, A.J., 2021. Anatomy of strike-slip fault tsunami genesis, *Proc. Natl. Acad. Sci.,* **118**(19), e2025632118, doi:10.1073/pnas.2025632118.

Eyov, E., Klar, A., Kadri, U. & Stiassnie, M., 2013. Progressive waves in a compressible-ocean with an elastic bottom, *Wave Motion,* **50**(5), 929–939.

Fujii, Y. & Satake, K., 2007. Tsunami source of the 2004 Sumatra–Andaman earthquake inferred from tide gauge and satellite data, *Bull. seism. Soc. Am.,* **97**(1A), S192–S207.

Goda, K., Petrone, C., De Risi, R. & Rossetto, T., 2017. Stochastic coupled simulation of strong motion and tsunami for the 2011 Tohoku, Japan earthquake, *Stoch. Environ. Res. Risk Assess.,* **31**(9), 2337–2355.

Grezio, A. *et al.*, 2017. Probabilistic tsunami hazard analysis: multiple sources and global applications, *Rev. Geophys.,* **55**(4), 1158–1198.

Harris, R.A. *et al.*, 2011. Verifying a computational method for predicting extreme ground motion, *Seismol. Res. Lett.,* **82**(5), 638–644.

Harris, R.A. *et al.*, 2018. A suite of exercises for verifying dynamic earthquake rupture codes, *Seismol. Res. Lett.,* **89**(3), 1146–1162.

Hayes, G.P., McNamara, D.E., Seidman, L. & Roger, J., 2014. Quantifying potential earthquake and tsunami hazard in the lesser Antilles subduction zone of the Caribbean region, *Geophys. J. Int.,* **196**(1), 510–521.

Kajiura, K., 1963. The leading wave of a tsunami, *Bull. Earthq. Res. Inst., Univ. Tokyo,* **41**(3), 535–571.

Kajiura, K., 1970. Tsunami source, energy and the directivity of wave radiation, *Bull. Earthq. Res. Inst.,* **48,** 835–869.

Kawaguchi, K., Kaneda, Y. & Araki, E., 2008. The DONET: a real-time seafloor research infrastructure for the precise earthquake and tsunami monitoring, in *OCEANS 2008-MTS/IEEE Kobe Techno-Ocean,* pp. 1–4, IEEE.

Kervella, Y., Dutykh, D. & Dias, F., 2007. Comparison between three-dimensional linear and nonlinear tsunami generation models, *Theor. Comput. Fluid Dyn.,* **21**(4), 245–269.

Kozdon, J.E. & Dunham, E.M., 2013. Rupture to the trench: dynamic rupture simulations of the 11 March 2011 Tohoku earthquake, *Bull. seism. Soc. Am.,* **103**(2B), 1275–1289.

Kozdon, J.E. & Dunham, E.M., 2014. Constraining shallow slip and tsunami excitation in megathrust ruptures using seismic and ocean acoustic waves recorded on ocean-bottom sensor networks, *Earth planet. Sci. Lett.,* **396,** 56–65.

Kozdon, J.E., Dunham, E.M. & Nordström, J., 2012. Interaction of waves with frictional interfaces using summation-by-parts difference operators: weak enforcement of nonlinear boundary conditions, *J. Sci. Comput.,* **50**(2), 341–367.

Kozdon, J.E., Dunham, E.M. & Nordström, J., 2013. Simulation of dynamic earthquake ruptures in complex geometries using high-order finite difference methods, *J. Sci. Comput.,* **55**(1), 92–124.

Krenz, L., Uphoff, C., Ulrich, T., Gabriel, A.-A., Abrahams, L.S., Dunham, E.M. & Bader, M., 2021. 3D acoustic-elastic coupling with gravity: the dynamics of the 2018 Palu, Sulawesi earthquake and tsunami, in *Proceedings of the International Conference for High Performance Computing, Networking, Storage and Analysis,* pp. 1–14.

Kubota, T., Saito, T., Fukao, Y., Sugioka, H., Ito, A., Tonegawa, T., Shiobara, H. & Yamashita, M., 2021. Earthquake rupture and tsunami generation of the 2015 Mw 5.9 Bonin event revealed by in situ pressure gauge array observations and integrated seismic and tsunami wave simulation, *Geophys. Res. Lett.,* **48**(22), e2021GL095915, doi:10.1029/2021GL095915.

Lay, T., 2018. A review of the rupture characteristics of the 2011 Tohoku-Oki Mw 9.1 earthquake, *Tectonophysics,* **733,** 4–36.

Lay, T., Yamazaki, Y., Ammon, C.J., Cheung, K.F. & Kanamori, H., 2011. The 2011 Mw 9.0 off the Pacific coast of Tohoku earthquake: comparison of deep-water tsunami signals with finite-fault rupture model predictions, *Earth, Planets Space,* **63**(7), 797–801.

LeVeque, R.J., Waagan, K., González, F.I., Rim, D. & Lin, G., 2016. Generating random earthquake events for probabilistic tsunami hazard assessment, in *Global Tsunami Science: Past and Future,* Vol. I, pp. 3671–3692, Springer.

Levin, B.W., Nosov, M., *et al.*, 2009. *Physics of Tsunamis,* Vol. 327, Springer.

Lindsey, N.J., Dawe, T.C. & Ajo-Franklin, J.B., 2019. Illuminating seafloor faults and ocean dynamics with dark fiber distributed acoustic sensing, *Science,* **366**(6469), 1103–1107.

Liu, P. L.-F., Wang, X. & Salisbury, A.J., 2009. Tsunami hazard and early warning system in South China Sea, *J. Asian Earth Sci.,* **36**(1), 2–12.

Lotto, G.C. & Dunham, E.M., 2015. High-order finite difference modeling of tsunami generation in a compressible ocean from offshore earthquakes, *Comput. Geosci.,* **19**(2), 327–340.

Lotto, G.C., Jeppson, T.N. & Dunham, E.M., 2018. Fully coupled simulations of megathrust earthquakes and tsunamis in the Japan Trench, Nankai Trough, and Cascadia subduction zone, *Pure appl. Geophys.,* **176,** 4009–4041.

Lotto, G.C., Nava, G. & Dunham, E.M., 2017. Should tsunami simulations include a nonzero initial horizontal velocity?, *Earth, Planets Space,* **69**(1) , doi:10.1186/s40623-017-0701-8.

Ma, S., 2022. Dynamic off-fault failure and tsunamigenesis at strike-slip restraining bends: fully-coupled models of dynamic rupture, ocean acoustic waves, and tsunami in a shallow bay, *Tectonophysics,* **838,** doi:10.1016/j.tecto.2022.229496.

Madden, E.H. *et al.*, 2021. Linked 3-D modelling of megathrust earthquake-tsunami events: from subduction to tsunami run up, *Geophys. J. Int.,* **224**(1), 487–516.

Maeda, T. & Furumura, T., 2013. FDM simulation of seismic waves, ocean acoustic waves, and tsunamis based on tsunami-coupled equations of motion, *Pure appl. Geophys.,* **170**(1–2), 109–127.

Matsumoto, H., Nosov, M.A., Kolesov, S.V. & Kaneda, Y., 2017. Analysis of pressure and acceleration signals from the 2011 Tohoku earthquake observed by the DONET seafloor network, *J. Disaster Res.,* **12**(1), 163–175.

Meyers, R.A., 2001. *Encyclopedia of Physical Science and Technology,* 3rd edn, Academic Press Inc.

Mulia, I.E., Heidarzadeh, M. & Satake, K., 2022. Effects of depth of fault slip and continental shelf geometry on the generation of anomalously long-period tsunami by the July 2020 Mw 7.8 Shumagin (Alaska) earthquake, *Geophys. Res. Lett.,* **49**(3), e2021GL094937, doi:10.1029/2021GL094937.

Nakamura, T., Takenaka, H., Okamoto, T. & Kaneda, Y., 2012. Fdm simulation of seismic-wave propagation for an aftershock of the 2009 suruga bay earthquake: effects of ocean-bottom topography and seawater layer, *Bull. seism. Soc. Am.,* **102**(6), 2420–2435.

Noguchi, S., Maeda, T. & Furumura, T., 2016. Ocean-influenced Rayleigh waves from outer-rise earthquakes and their effects on durations of long-period ground motion, *Geophys. J. Int.,* **205**(2), 1099–1107.

Nosov, M., 1999. Tsunami generation in compressible ocean, *Phys. Chem. Earth, Part B,* **24**(5), 437–441.

Nosov, M. & Kolesov, S., 2007. Elastic oscillations of water column in the 2003 Tokachi-oki tsunami source: in-situ measurements and 3-D numerical modelling, *Nat. Hazards Earth Syst. Sciences,* **7**(2), 243–249.

Nosov, M.A. & Kolesov, S.V., 2011. Optimal initial conditions for simulation of seismotectonic tsunamis, *Pure appl. Geophys.,* **168**(6), 1223–1237.

Okada, Y., 1985. Surface deformation due to shear and tensile faults in a half-space, *Bull. seism. Soc. Am.,* **75**(4), 1135–1154.

Pelties, C., Gabriel, A.A. & Ampuero, J.P., 2014. Verification of an ADER-DG method for complex dynamic rupture problems, *Geosci. Model Dev.,* **7,** 847–866.

Press, F., Ewing, M. & Tolstoy, I., 1950. The airy phase of shallow-focus submarine earthquakes, *Bull. seism. Soc. Am.,* **40**(2), 111–148.

Saito, T., 2019. Chapter 5: Tsunami generation and propagation, in *Tsunami Generation,* Springer.

Saito, T., Baba, T., Inazu, D., Takemura, S. & Fukuyama, E., 2019. Synthesizing sea surface height change including seismic waves and tsunami using a dynamic rupture scenario of anticipated Nankai trough earthquakes, *Tectonophysics,* **769,** doi:10.1016/j.tecto.2019.228166.

Saito, T. & Furumura, T., 2009. Three-dimensional tsunami generation simulation due to sea-bottom deformation and its interpretation based on the linear theory, *Geophys. J. Int.,* **178**(2), 877–888.

Saito, T. & Kubota, T., 2020. Tsunami modeling for the deep sea and inside focal areas, *Ann. Rev. Earth planet. Sci.,* **48,** 121–145.

Saito, T., Satake, K. & Furumura, T., 2010. Tsunami waveform inversion including dispersive waves: the 2004 earthquake off Kii Peninsula, Japan, *J. geophys. Res.,* **115**(B6), doi:10.1029/2009JB006884.

Saito, T. & Tsushima, H., 2016. Synthesizing ocean bottom pressure records including seismic wave and tsunami contributions: toward realistic tests of monitoring systems, *J. geophys. Res.,* **121**(11), 8175–8195.

Satake, K., Fujii, Y., Harada, T. & Namegaya, Y., 2013. Time and space distribution of coseismic slip of the 2011 Tohoku earthquake as inferred from tsunami waveform data, *Bull. seism. Soc. Am.,* **103**(2B), 1473–1492.

Scala, A. *et al.*, 2020. Effect of shallow slip amplification uncertainty on probabilistic tsunami hazard analysis in subduction zones: use of long-term balanced stochastic slip models, *Pure appl. Geophys.,* **177**(3), 1497–1520.

Sells, C.L., 1965. The effect of a sudden change of shape of the bottom of a slightly compressible ocean, *Phil. Trans. R. Soc. Lond., A,* **258**(1092), 495–528.

Selva, J. *et al.*, 2021. Probabilistic tsunami forecasting for early warning, *Nat. Commun.,* **12**(1), 1–14.

Simons, M. *et al.*, 2011. The 2011 magnitude 9.0 Tohoku-Oki earthquake: mosaicking the megathrust from seconds to centuries, *Science,* **332**(6036), 1421–1425.

Sladen, A., Rivet, D., Ampuero, J.P., De Barros, L., Hello, Y., Calbris, G. & Lamare, P., 2019. Distributed sensing of earthquakes and ocean-solid Earth interactions on seafloor telecom cables, *Nat. Commun.,* **10**(1), 1–8.

Song, Y.T., Fu, L.L., Zlotnicki, V., Ji, C., Hjorleifsdottir, V., Shum, C.K. & Yi, Y., 2008. The role of horizontal impulses of the faulting continental slope in generating the 26 December 2004 tsunami, *Ocean Modell.,* **20**(4), 362–379.

Song, Y.T. & Han, S.-C., 2011. Satellite observations defying the long-held tsunami genesis theory, in *Remote Sensing of the Changing Oceans,* ed. Tang, D., Springer.

Song, Y.T., Mohtat, A. & Yim, S.C., 2017. New insights on tsunami genesis and energy source, *J. geophys. Res.,* **122**(5), 4238–4256.

Stoneley, R., 1926. The effect of the ocean on Rayleigh waves, *Geophys. Suppl. Mon. Not. R. astron. Soc.,* **1**(7), 349–356.

Sugioka, H. *et al.*, 2012. Tsunamigenic potential of the shallow subduction plate boundary inferred from slow seismic slip, *Nat. Geosci.,* **5**(6), 414–418.

Takagi, R., Toyokuni, G. & Chikasada, N., 2021. Ambient noise correlation analysis of s-net records: extracting surface wave signals below instrument noise levels, *Geophys. J. Int.,* **224**(3), 1640–1657.

Takemura, S., Kimura, T., Saito, T., Kubo, H. & Shiomi, K., 2018. Moment tensor inversion of the 2016 southeast offshore Mie earthquake in the Tonankai region using a three-dimensional velocity structure model: effects of the accretionary prism and subducting oceanic plate, *Earth, Planets Space,* **70**(1), 1–19.

Takeo, A., Forsyth, D.W., Weeraratne, D.S. & Nishida, K., 2014. Estimation of azimuthal anisotropy in the NW Pacific from seismic ambient noise in seafloor records, *Geophys. J. Int.,* **199**(1), 11–22.

Tanioka, Y. & Sataka, K., 1996a. Fault parameters of the 1896 Sanriku tsunami earthquake estimated from tsunami numerical modeling, *Geophys. Res. Lett.,* **23**(13), 1549–1552.

Tanioka, Y. & Satake, K., 1996b.Tsunami generation by horizontal displacement of ocean bottom, *Geophys. Res. Lett.,* **23**(8), 861–864.

Tanioka, Y. & Seno, T., 2001. Sediment effect on tsunami generation of the 1896 Sanriku tsunami earthquake, *Geophys. Res. Lett.,* **28**(17), 3389–3392.

Todoriki, M., Furumura, T. & Maeda, T., 2016. Effects of seawater on elongated duration of ground motion as well as variation in its amplitude for offshore earthquakes, *Geophys. J. Int.,* **208**(1), 226–233.

Tsushima, H., Hino, R., Tanioka, Y., Imamura, F. & Fujimoto, H., 2012. Tsunami waveform inversion incorporating permanent seafloor deformation and its application to tsunami forecasting, *J. geophys. Res.,* **117**(B3), doi:10.1029/2011JB008877.

Ulrich, T. *et al.*, 2019. Coupled, physics-based modeling reveals earthquake displacements are critical to the 2018 Palu, Sulawesi tsunami, *Pure appl. Geophys.,* **176**(10), 4069–4109.

Uphoff, C., Rettenberger, S., Bader, M., Madden, E.H., Ulrich, T., Wollherr, S. & Gabriel, A.-A., 2017. Extreme scale multi-physics simulations of the tsunamigenic 2004 Sumatra megathrust earthquake, in *Proceedings of the international conference for high performance computing, networking, storage and analysis,* pp. 1–16.

Ward, S.N., 1980. Relationships of tsunami generation and an earthquake source, *J. Phys. Earth,* **28**(5), 441–474.

Ward, S.N., 1981. On tsunami nucleation: 1. A point source, *J. geophys. Res.,* **86**(B9), 7895–7900.

Wilson, A. & Ma, S., 2021. Wedge plasticity and fully coupled simulations of dynamic rupture and tsunami in the Cascadia subduction zone, *J. geophys. Res.,* **126**(7), e2020JB021627, doi:10.1029/2020JB021627.

Witter, R.C., Zhang, Y.J., Wang, K., Priest, G.R., Goldfinger, C., Stimely, L., English, J.T. & Ferro, P.A., 2013. Simulated tsunami inundation for a range of Cascadia megathrust earthquake scenarios at bandon, oregon, usa, *Geosphere,* **9**(6), 1783–1803.

Yamamoto, N., Hirata, K., Aoi, S., Suzuki, W., Nakamura, H. & Kunugi, T., 2016. Rapid estimation of tsunami source centroid location using a dense offshore observation network, *Geophys. Res. Lett.,* **43**(9), 4263–4269.

Yamazaki, Y., Cheung, K.F. & Lay, T., 2018. A self-consistent fault slip model for the 2011 Tohoku earthquake and tsunami, *J. geophys. Res.,* **123**(2), 1435–1458.

Ye, L., Bai, Y., Si, D., Lay, T., Cheung, K.F. & Kanamori, H., 2022. Rupture model for the 29 July 2021 Mw 8.2 Chignik, Alaska earthquake constrained by seismic, geodetic, and tsunami observations, *J. geophys. Res.,* **127**(7), e2021JB023676, doi:10.1029/2021JB023676.

Yokota, Y., Koketsu, K., Fujii, Y., Satake, K., Sakai, S., Shinohara, M. & Kanazawa, T., 2011. Joint inversion of strong motion, teleseismic, geodetic, and tsunami datasets for the rupture process of the 2011 Tohoku earthquake, *Geophys. Res. Lett.,* **38**(7), doi:10.1029/2011GL050098.

Zhan, Z., Cantono, M., Kamalov, V., Mecozzi, A., Müller, R., Yin, S. & Castellanos, J.C., 2021. Optical polarization–based seismic and water wave sensing on transoceanic cables, *Science,* **371**(6532), 931–936.

APPENDIX: VERIFICATION OF 3-D FULLY COUPLED METHOD

In this appendix, we present a computational verification test to ensure the correct implementation of the modified free surface boundary condition with gravity in the 3-D code SeisSol. To do this, we compare the numerical solution against analytical eigenmode solutions for the ocean response, obtained by extending the 2-D solution of Lotto & Dunham (2015) and Wilson & Ma (2021) to 3-D.

The eigenmode solution is obtained for a compressible ocean in the shape of a cuboid of height H and horizontal widths L_x and L_y (Fig. A1). The pressure is set to zero on the sides, the bottom is rigid ($v_z = 0$), and on the top we enforce eqs (6) and (7). Using standard techniques for solving linear, constant coefficient differential equations (e.g. Aki & Richards 2002), we seek a standing wave solution to the homogeneous eqs (2)–(5) and boundary conditions with horizontal wavenumbers k_x and k_y and angular frequency ω. The solution, which can also be obtained via rotation of the 2-D Lotto & Dunham (2015) solution about the z-axis, is

$$p(x,y,z,t) = \sin(k_x x)\sin(k_y y)\sin(\omega t) \times \left(\sinh(k^* z) + g\frac{k^*}{\omega^2}\cosh(k^* z)\right), \tag{A1}$$

$$v_x(x,y,z,t) = \frac{k_x}{\omega\rho}\cos(k_x x)\sin(k_y y)\cos(\omega t) \times \left(\sinh(k^* z) + g\frac{k^*}{\omega^2}\cosh(k^* z)\right), \tag{A2}$$

$$v_y(x,y,z,t) = \frac{k_y}{\omega\rho}\sin(k_x x)\cos(k_y y)\cos(\omega t) \times \left(\sinh(k^* z) + g\frac{k^*}{\omega^2}\cosh(k^* z)\right), \tag{A3}$$

$$v_z(x,y,z,t) = \frac{k^*}{\omega\rho}\sin(k_x x)\sin(k_y y)\cos(\omega t) \times \left(\cosh(k^* z) + g\frac{k^*}{\omega^2}\sinh(k^* z)\right), \tag{A4}$$

and

$$\eta(x,y,t) = \frac{k^*}{\omega^2\rho}\sin(k_x x)\sin(k_y y)\sin(\omega t), \tag{A5}$$

with

$$k^* = \sqrt{k_x^2 + k_y^2 - \frac{\omega^2}{c_0^2}}. \tag{A6}$$

The dispersion relation

$$\omega^2 = g k^* \tanh(k^* H) \tag{A7}$$

relates angular frequency and wavenumbers. The finite horizontal extent of the ocean, with pressure vanishing on the sides, leads to a discrete spectrum for the horizontal wavenumbers:

$$k_x = m_x\pi/L_x, \quad m_x = 0, 1, \ldots; \qquad k_y = m_y\pi/L_y, \quad m_y = 0, 1, \ldots. \tag{A8}$$

Next, we use this analytical eigenmode solution to set the initial pressure, particle velocities and sea surface height in a numerical simulation. We select $L_x = L_y = 10$ km, $H = 1$ km, and $m_x = m_y = 1$; ρ, c_0 and g are the same as in Table 2. Then we solve the dispersion relation (A7) for ω. There is an infinite number of solutions, which we index by n, with $n = 0$ being the surface gravity wave mode and $n = 1, 2, \ldots$ being the acoustic modes. Here we show results for $n = 0$, 1 and 2.

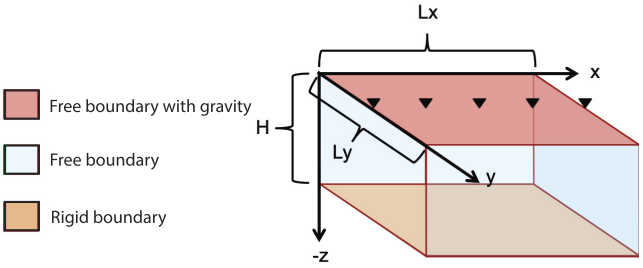

Figure A1. Eigenmode problem used for verification.

The domain is 10 km by 10 km in the horizontal direction with depth $H = 1$ km. For the base refinement the domain is divided into 100 (10 by 10) equal-sized boxes with 6 tetrahedral elements per box. Therefore, the domain's base level of resolution has 600 equally sized elements. We refine (in each direction and in time) by a factor of 2, 4, 8, 16 and 32 for each higher refinement level. Each successive refinement level therefore has $2^3 = 8$ times more elements than the previous refinement level. We evaluate polynomial orders 2, 4 and 6 within each element. The problem runs for one oscillation period (i.e. to final time $t = 2\pi/\omega$).

We compute the L_2 norm of the error in pressure over the 3-D domain at this final time. It is standard in the verification of numerical solutions to partial differential equations to quantify error at some final time with a norm taken over space. Convergence of this measure of error requires that both spatial discretization and time stepping are correctly implemented, so the test is sufficient to demonstrate accuracy. Fig. A2 and Tables A1–A3 show the results. The calculated convergence rates match the expected order of accuracy except at extremely high refinement levels for the high order cases, which we speculate is due to the onset of round-off error.

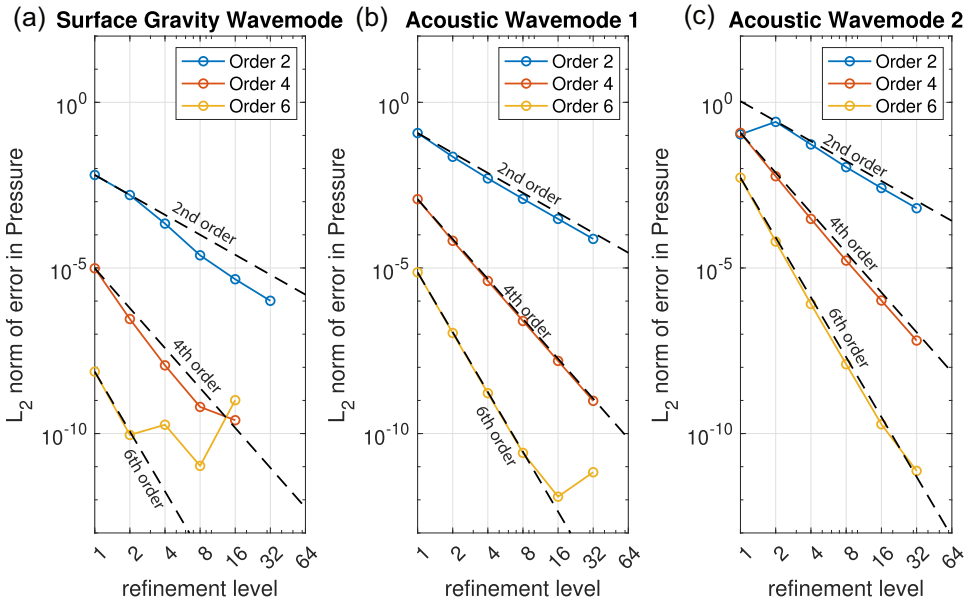

Figure A2. Convergence results for eigenmode verification study.

Table A1. Gravity wave mode ($n = 0$) convergence rate table.

Mode 0	Order 2		Order 4		Order 6	
Refinement Level	Error	Rate	Error	Rate	Error	Rate
1	6.4079e-03		9.7417e-06		7.3848e-09	
2	1.5877e-03	2.0129	2.8730e-07	5.0835	9.0906e-11	6.3440
4	2.1795e-04	2.8649	1.1462e-08	4.6476	1.8458e-10	−1.0218
8	2.4062e-05	3.1792	6.3695e-10	4.1696	1.0562e-11	4.1273
16	4.5579e-06	2.4003	2.5302e-10	1.3319	1.0187e-09	−6.5917
32	1.0200e-06	2.1599	-*	-*	-*	-*

*Not run due to computational expense.

Table A2. Acoustic wave mode ($n = 1$) convergence rate table.

Mode 1	Order 2		Order 4		Order 6	
Refinement level	Error	Rate	Error	Rate	Error	Rate
1	1.1800e-01		1.1889e-03		7.3651e-06	
2	2.2707e-02	2.3776	6.6027e-05	4.1704	1.0851e-07	6.0848
4	5.0400e-03	2.1716	4.0673e-06	4.0209	1.6614e-09	6.0293
8	1.2196e-03	2.047	2.5038e-07	4.0219	2.6089e-11	5.9928
16	3.0241e-04	2.0118	1.5616e-08	4.003	1.2432e-12	4.3914
32	7.5284e-05	2.0061	9.7317e-10	4.0042	6.8058e-12	−2.4528

Table A3. Acoustic wave mode ($n = 2$) convergence rate table.

Mode 2	Order 2		Order 4		Order 6	
Refinement level	Error	Rate	Error	Rate	Error	Rate
1	1.0791e-01		1.1970e-01		5.3067e-03	
2	2.5684e-01	-1.2511	5.8573e-03	4.353	6.2510e-05	6.4076
4	5.3644e-02	2.2594	3.0234e-04	4.276	8.1661e-07	6.2583
8	1.1045e-02	2.28	1.6683e-05	4.1797	1.2381e-08	6.0434
16	2.588e-03	2.0936	1.0406e-06	4.0029	1.9104e-10	6.0181
32	6.3474e-04	2.0276	6.4365e-08	4.015	7.4649e-12	4.6776